ATLAS PUB Note

ATL-PHYS-PUB-2025-035

17th September 2025

Reference Single Top-Quark Cross-Sections for ATLAS and CMS Analyses

The ATLAS and CMS Collaborations

This note presents reference cross-sections and recommendations for the evaluation of uncertainties in the three main single top-quark production-processes of the Standard Model. Cross-sections are calculated up to next-to-next-to-leading order in QCD pertubation theory for all relevant centre-of-mass energies. For all channels dependencies of the cross-section as function of the top-quark mass and the centre-of-mass energy are provided. For dominant process, the single top-quark production in the t-channel comprehensive comparisons with cross-sections calculated with several parton distribution functions are performed.

1 Introduction

Since the start of the Large Hadron Collider (LHC), proton–proton (pp) collisions at centre-of-mass energy of $\sqrt{s} =$ 5.02 TeV, 13 TeV and 13.6 TeV, have been provided to the collider experiments with access to a previously unexplored kinematic range, effectively turning the LHC into a top-quark factory. Top quarks are produced singly via weak charged-current interactions. At leading order (LO) in QCD perturbation theory, single top-quark production is described by three subprocesses. The dominant process is the t-channel exchange of a W boson, depicted in Figure 1(a) and denoted as the $tq + \bar{t}q$ process. The subleading single top-quark processes are the associated production of a W boson and a top quark (tW), depicted in Figure 1(b) and the single top-quark production with a virtual s-channel W boson, denoted as the $t\bar{b} + \bar{t}b$ process and depicted in Figure 1(c) which is analogous to the Drell–Yan process. Since both, the production of single top-quark events via the t-channel and the s-channel are charge asymmetric - due to different quark flavours for top-quark and top-antiquark production in the initial state - separate cross-sections for top-quark and top-antiquark production are provided. This charge asymmetry can be encoded as the ratio of the cross-section for the tq production to the cross-section of the $\bar{t}q$ production, denoted as R_t. In contrast, the tW is charge symmetric, and thus a common cross-section is reported.

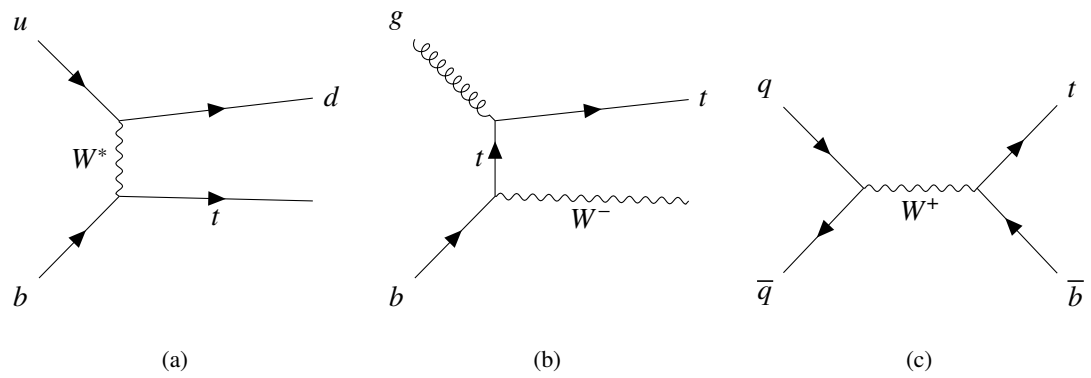

(a) (b) (c)

Figure 1: Representative leading-order Feynman diagrams of (a) t-channel single top-quark production, (b) associated tW production, and (c) s-channel single top-quark production.

In 2014-2015, the goal was to provide a common inclusive reference cross-section for single-top-quark processes to be used by the ATLAS and CMS collaborations. For this, a fast parameterisation of cross-sections with next-to-leading order (NLO) accuracy in QCD pertubation theory were provided by Hathor [1] or calculations provided by theorists were used. In recent years, next-to-next-to-leading order (NNLO) calculations in QCD perturbation theory for t- and the s-channel single top-quark production and improved soft-gluon corrections at approximate N^{3}LO accury became available [2–6] together with improved parton distribution functions (PDFs). Thus, it is important to update reference cross-sections used by both collaborations. With the availability of the NNLO calculation in MCFM [7] for the t-channel process, it is possible for experimentalists and phenomenologists to calculate cross-section predictions for various parameter choices. In particular dependencies of the top-quark mass (m_{top}) and of the centre-of-mass energy can easily be provided. For higher-order cross-sections of the associated tW production and the s-channel single top-quark production the predictions are provided directly by the authors [5, 6].

2 Theoretical uncertainties and parameter dependencies

This section outlines the theoretical uncertainties considered, including PDF uncertainties, the choice of renormalisation and factorisation scales, and variations of string coupling constant α_s. A short overview of the PDFs used is presented and finally the parametrisation of cross-sections for different top-quark masses and beam energies is discussed. For the tW and s-channel production modes, the cross-section values rely on results provided directly by the authors; as a result, uncertainty prescriptions might differ from the proposed procedures and not all uncertainty components can be detailed for these two processes.

2.1 Statistical uncertainty

The statistical uncertainty on all cross-section calculations is below 0.2% and therefore considered negligible. This is also assumed for the values provided by the authors.

2.2 PDF+ α_s uncertainty

Parton distribution functions describe the probability of finding a parton inside a hadron as a function of the fraction x of the proton's momentum carried by the parton. PDF sets are determined by performing global fits to a large number of measured cross-sections across a broad range of Q^2 and x values from multiple experiments. The standard approach is to parameterise the x-dependence of the parton distributions at a low input scale $Q^2 = Q_0^2$, and subsequently evolve these distributions to higher Q^2 values using the DGLAP equations. PDF sets are available from various groups worldwide, e.g. ABM [8], CTEQ-TEA [9], MSHT [10], NNPDF [11–13], and HERAPDF [14]. The ATLAS collaboration also provides its own PDF sets [15–17]. The PDFs provided by the different groups differ in the data used in the fit, the value of α_s, and the values of (heavy) quark masses as well as how heavy quark effects are taken into account. They also differ in the way higher order perturbative QCD corrections are implemented, the parametrisation form, the way of treating systematic uncertainties, and the criteria for estimating confidence levels.

The nominal PDF set used for the cross-section recommendations are the PDF4LHC21 sets, which are a combined effort of the CTEQ-TEA, MSHT, and NNPDF collaborations. In addition, cross-sections values are provided - where available - for the most recent individual PDF sets as well as for a few previous versions. From the CTEQ-TEA group the CT18 PDF set and from the MSHT group the MSHT2020 set are considered. From the NNPDF group the most recent PDF set NNPDF4.0 and the predecessors NNPDF3.0 and NNPDF3.1 are used. NNPDF3.0 is included since it is still the default PDF set for event generation in ATLAS. Additionally, values for ABM16 and the all experiment PDF sets namely ATLAS epWZ16, ATLAS epWZtop18, ATLAS epWZVjet20 and ATLASpdf21 produced by the ATLAS collaboration are provided. In contrast to all other PDF sets, the ATLAS PDF sets used here are based only on deep inelastic scattering data from ep collisions at the HERA collider and ATLAS data.

Table 1 summarizes the considered PDF sets together with their central α_s value and the experiments from which the fitted data are used. The ratio of t-channel top-quark to top-antiquark production cross-sections, R_t, offers a framework, to test predictions from these different PDF sets, since R_t is sensitive to the momentum probability density of quarks in the proton. From the leading-order Feynman diagram of the t-channel process (see Figure 3), one can see that the initial state consists of a light quark and a b-quark. The charge of the light quark is directly connected to the charge of the W boson coming from the top-quark or top-antiquark decay. The charge of the lepton from the subsequent W-boson decay indicates whether the

Table 1: List of PDFs together with their used α_s value and the list the experiments from which data are included in the fits.

PDF set	Order	$\alpha_s(m_Z)$	Experiments
ABM16 (5 flav.)	NNLO	0.115	Combined HERA, Fixed target
ATLAS (epWZ16)	NNLO	0.118	Combined HERA, ATLAS W, Z
ATLAS (epWZtop18)	NNLO	0.118	Combined HERA, ATLAS W, Z + top
ATLAS (epWZVjet20)	NNLO	0.118	Combined HERA, ATLAS W, Z + jet data
ATLASpdf21	NNLO	0.118	Combined HERA, ATLAS W, Z + jet data + top
CT18	NNLO	0.118	Combined HERA, Fixed target, Tevatron, LHC
MSHT2020	NNLO	0.118	Combined HERA, Fixed target, Tevatron, LHC
NNPDF3.0	NNLO	0.118	Combined HERA, Fixed target, Tevatron, LHC
NNPDF3.1	NNLO	0.118	Combined HERA, Fixed target, Tevatron, LHC
NNPDF4.0	NNLO	0.118	Combined HERA, Fixed target, Tevatron, LHC
PDF4LHC21	NNLO	0.118	Meta PDF based on CT18, MSHT2020, NNPDF3.1

initial light quark was an up-type or a down-type. In t-channel single top-quark production, the initial light quark has a momentum fraction large enough to produce a massive top-quark. Figure 2 shows the fraction of events with a valence u-quark or a valence d-quark, which dominate at high X, as a function of their momentum fraction x. The u-quark typically appears in the initial state for top-quark production, while the d-quark appears in the initial state for top-antiquark production. The distribution for the u-quark is shifted towards higher values of x than for the d-quark, reflecting that there is a higher probability for a valence u-quark than for a valence d-quark to participate in the hard interaction. Uncertainties connected with the

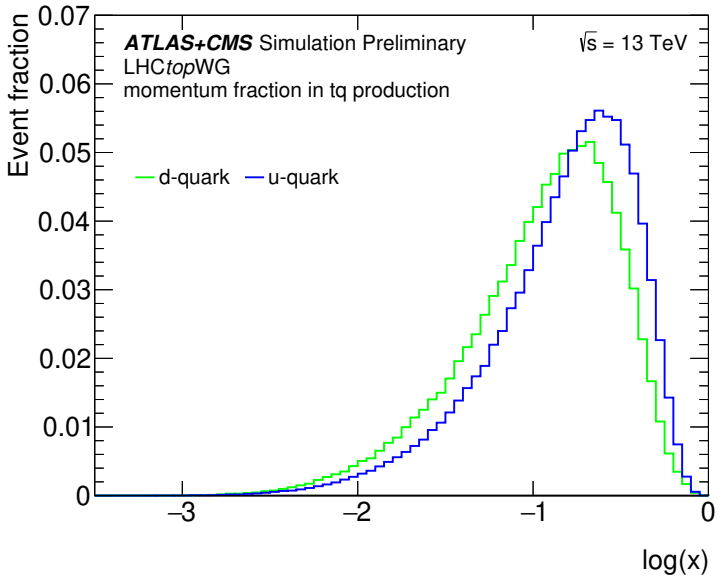

Figure 2: Fraction of events with an u-quark or a d-quark as a function of their momentum fraction x in t-channel single top-quark events at $\sqrt{s}$ = 13 TeV. The u-quark belongs to the initial state parton in top-quark processes, while the d-quark is the initial state in the top-antiquark process. The calculations are performed using POWHEG [18, 19] at NLO.

determination of the PDFs themselves are evaluated using the corresponding prescription. For almost all PDF sets the formula given in Eq. 43 from Ref. [20] is used:

$$\Delta X^{+}_{\mathrm{max}} = \sqrt{\sum_{i=1}^{N} [\max(X_i^{+} - X_0, X_i^{-} - X_0, 0)]^2}$$
$$\Delta X^{-}_{\mathrm{max}} = \sqrt{\sum_{i=1}^{N} [\max(X_0 - X_i^{+}, X^0 - X_i^{-}, 0)]^2} \quad (1)$$

Here X is some observable, such as the cross-section or the cross-section ratio R_t, the subscript 0 denotes the nominal value, the superscript indicates using a PDF variation in the "+ direction" and in the "- direction". $\Delta X^{+}_{\mathrm{max}}$ adds in quadrature the PDF variations that lead to an increase of the quantity while $\Delta X^{-}_{\mathrm{max}}$ adds in quadrature those that lead to a decrease. In case of the NNPDF sets the internal uncertainty is determined differently, namely by using an ensemble of pseudo-experiments (replicas) and calculation the RMS to obtain the uncertainties, as described in [12]. It was been shown that a Hessian representation obtained from the replicas gives similar results [21]. In the Hessian method, a parametrisation with fixed functions and a multigaussian probability distribution for the parameter space is assumned. Uncertainties are then given as the inverse of the covariance matrix. Since the uncertainties for PDF sets from the CTEQ-TEA group are provided at 90% C.L., whereas all others are given at 68% C.L. the resulting CTEQ-TEA uncertainty is divided by 1.645 [22].

Since the value of the cross-sections depends also on the choice of α_s, an uncertainty on α_s is taken into account by varying it by ±0.01 around the nominal value. As the central value for determining the α_s uncertainty, the corresponding PDF set with $\alpha_s(m_Z) = 0.118$ ($\alpha_s(m_Z) = 0.115$ for ABM) is used. The uncertainty is then estimated comparing the central value with the PDF set using a varied $\alpha_s(m_Z) = 0.118 \pm 0.01$ ($\alpha(m_Z)s = 0.115 \pm 0.01$ for ABM) value in the fit.

2.3 Renormalisation and factorisation scale uncertainties

Scale uncertainties are typically estimated by varying the renormalisation scale μ_r and the factorization scale μ_f simultaneously by a factor one half or two. This is an estimate for uncertainties due to missing higher-order perturbative corrections. A more comprehensive way of estimating scale uncertainties is to vary μ_r and μ_f independently up and down by a factor of two whilst never allowing them to differ by a factor greater than two from each other - so-called independent restricted scale variations. The uncertainty is then defined by the difference between the maximum value of the cross-sections and the nominal cross-section as up variation and the difference between the minimal cross-section and the nominal cross-section as down variation. The uncertainties are estimated separately for top-quark and top-antiquark production in the case of t- and s-channel production. The methods used differ between processes and are specified in the corresponding process descriptions. Exemplary values for the scale variation procedure using the PDF4LHC21 PDF set are shown in Table 2 for the $tq + \bar{t}q$ process.

2.4 Additional uncertainties and dependencies

The following uncertainties are provided for use in measurements sensitive to single top cross section, where relevant. Variations in the top-quark mass and beam energy are suggested, along with analytic dependencies of the production cross-section on the top-quark mass and center-of-mass energy.

μ_r	μ_f	$\sigma(tq)$ [pb]	$\sigma(\bar{t}q)$ [pb]
$\frac{1}{2}$	$\frac{1}{2}$	133.3	79.4
$\frac{1}{2}$	1	**133.1**	**79.2**
1	$\frac{1}{2}$	134.0	79.9
1	1	*134.2*	*80.0*
1	2	134.2	79.9
2	1	135.1	80.5
2	2	**135.7**	**80.8**

Table 2: The tq and $\bar{t}q$ cross-sections in pb for different scale choices at $\sqrt{s} = 13$ TeV using the PDF4LHC21 PDF set. The nominal ($\mu_r = \mu_f = 1$) cross-sections are shown in italic, while maximal and minimal cross-section values are indicated in bold.

Mass uncertainty To estimate the uncertainty in the assumed m_{top}, a variation of ± 1.0 GeV in the assumed m_{top} is assigned. The size of this variation is taken conservatively here. In general, the top-quark mass uncertainty is not included in the quoted total cross-section uncertainty, but is used for property measurements like the extraction of $|V_{tb}|$.

Beam energy uncertainty The LHC beam energy is known to be within 0.1% of the nominal value, based on the LHC magnetic model and comparisons of the revolution frequencies of proton and lead-ion beam [23]. Thus, to estimate the uncertainty a variation of $\pm 0.1\%$ in the $\sqrt{s}$ is applied. The beam energy uncertainty is then given by using the $\sqrt{s}$ dependence defined in Eq. (4) below.

$$\Delta\sigma_{\text{beam}} = \frac{d\sigma(\sqrt{s})}{d\sqrt{s}} \cdot 0.1\% \cdot \sqrt{s}. \tag{2}$$

Both beams are assumed to be 100% correlated, therefore the relative energy uncertainty of the pp centre-of-mass system stays the same. In general, the beam energy uncertainty is not treated as part of the quoted total uncertainty, but could be used for property measurements like the extraction of $|V_{tb}|$.

Top-quark mass and $\sqrt{s}$ dependence The single top-quark cross-sections show a strong dependence on m_{top} where the cross-sections decrease with increasing m_{top}. A parametrisation for the mass dependence as proposed in Ref. [24] for the $t\bar{t}$ cross-section can also be applied to single top-quark cross-sections. The reference top-quark mass m_{ref} is set to 172.5 GeV and the parametrisation takes the following form:

$$\sigma(m_{\text{top}}) = \sigma(m_{\text{ref}}) \cdot \left(\frac{m_{\text{ref}}}{m_{\text{top}}}\right)^4 \cdot \left[1 + a_1\left(\frac{m_{\text{top}} - m_{\text{ref}}}{m_{\text{ref}}}\right) + a_2\left(\frac{m_{\text{top}} - m_{\text{ref}}}{m_{\text{ref}}}\right)^2\right] \tag{3}$$

According to Ref. [24] this equation holds true and is accurate at the sub-percent level with m_{top} reaching from 130 - 210 GeV. Results for the parametrisation can be found for all the processes in the recommendation sections.

With increasing centre-of-mass energy the cross-sections for the single top-quark processes are increasing. A parametrisation for the dependence in $\sqrt{s}$ of hadronic inclusive cross-sections can be obtained via the following formula, as proposed in Ref. [25]:

$$\sigma(\sqrt{s}) = a_0 + \sqrt{s} \cdot \left[a_1 + a_3 \ln\left(\frac{\sqrt{s}}{14\,\text{TeV}}\right) + a_4 \ln^2\left(\frac{\sqrt{s}}{14\,\text{TeV}}\right)\right] + s \cdot \left[a_2 + a_5 \ln\left(\frac{\sqrt{s}}{14\,\text{TeV}}\right) + a_6 \ln^2\left(\frac{\sqrt{s}}{14\,\text{TeV}}\right)\right] \quad (4)$$

This form of parametrisation is consistent with unitarity and is justified by general limits for cross-sections at high-energies in a range of approximately $3\,\text{TeV} < \sqrt{s} < 14\,\text{TeV}$. The unit of the total cross-section, as a function of the centre-of-mass energy (CME) $\sqrt{s}$, is pb. Results for the parametrisation can be found for all the processes in the recommendation sections.

In the recommendations, the values of the parameters from Eq. (3) and Eq. (4) are quoted for all three sub-processes. The parameters are estimated by fitting to the corresponding cross-sections. To determine the parameters from Eq. (3), the cross-section is computed for different values of the top-quark mass and then used to fit the equation to determine the coefficients a_1 and a_2. To determine the parameters from Eq. (4), the cross-section computed for the different $\sqrt{s}$ values is fitted, obtaining the parameters a_0 to a_6.

3 t-channel single top-quark production

The NNLO perturbative QCD calculations for the t-channel process are performed separately for the

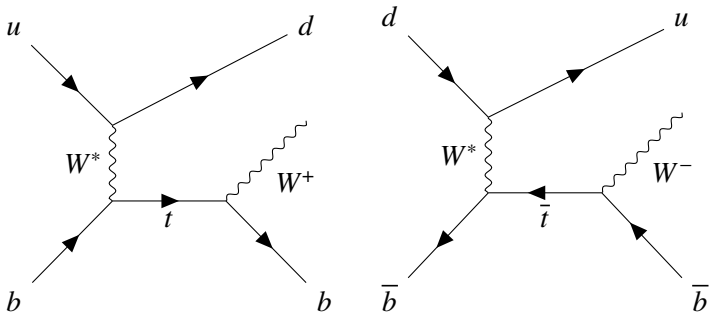

Figure 3: Representative leading-order Feynman diagrams of (a) single top-quark production and (b) single top-antiquark production via the t-channel exchange of a virtual W^* boson, including the decay of the top-quark and top-antiquark, respectively.

top-quark and top-antiquark cross-sections using MCFM [26], and are based on the calculation in Ref. [4]. Exemplary LO Feynman diagrams are shown in Figure 3). A new feature of this calculation is the reintroduction of the so-called dynamic double deep inelastic scattering (DDIS) scale [26] in order to account for higher missing orders. For the implementation of DDIS in MCFM the momentum transfer along the W Boson Q^2 is used as the scale for the light-quark line (ud-quark line) $\mu_r^2 = \mu_f^2 = Q^2$ and $\mu_r^2 = \mu_f^2 = Q^2 + m_t^2$ for the heavy-quark line (bottom-quark line) [7]. Although DDIS formally breaks down at NNLO in QCD pertubation theory, it can still be used due to the small expected interference between the light- and heavy-quark lines. This scale was used already in very early NLO calculations [27], whereas more recent calculations employed a fixed scale equal to m_{top}.

The calculation is done in the so-called G_F scheme, which is also the default setting in MCFM, with a fixed diagonal CKM matrix with $V_{ud} = V_{cs} = V_{tb} = 1$ and stable top-quarks, neither the decay nor any production–decay interference contributions are included. A summary of the most important parameters is presented in Table 3. Since the calculations are done in the five flavour-scheme (5FS) the quark masses are all set to zero except for the mass of the top quark. This follows the typical strategy for calculations of inclusive cross-sections for this process, while the event generation in MC simulation is done in the four flavour-scheme (4FS) to benefit from improved kinematics, especially for the spectator b-quark, i.e. the one coming from the initial gluon splitting. A detailed discussion about 4FS vs. 5FS calculations can be found in Ref. [28]. The PDF sets are included in the calculation using LHAPDF [29].

3.1 Cross-sections and their ratios for different PDFs

This section presents the predicted cross-sections for various PDF sets for $\sqrt{s} =$ 5.02 TeV, 13 TeV and 13.6 TeV. In addition, comparisons are shown between the NNLO and NLO calculations performed with MCFM at $\sqrt{s} =$ 13 TeV, and the NLO predictions from Hathor, which were used in the previous set of cross-section recommendations.

Table 3: List of parameters and their values used with MCFM to obtain the calculated t-channel cross-sections.

Parameter	Value	Comment
Process	1610	
ewscheme	1	
precisiongoal	0.005	
absprecisiongoal	50.0	
m_W	80.385 GeV	
$\Gamma(W)$	2.085 GeV	
m_Z	91.1876 GeV	
$\Gamma(Z)$	2.4952 GeV	
m_{top}	172.5 GeV	
m_b	0 GeV	
m_c	0 GeV	
G_F	$0.116639 \cdot 10^{-04}$	
$1/\alpha_{em}(m_Z)$	132.2319487	calculated
$\sin^2(\theta_w)$	0.2228972	calculated

3.1.1 NNLO cross-sections

Tables 4–15 list the cross-sections, their ratios, and their uncertainties for different PDF sets and different centre-of-mass energies. All uncertainties on tq and $\bar{t}q$ are treated as fully correlated. The cross-section values are summed for tq and $\bar{t}q$ at each variation point, and the uncertainty envelope is constructed, the same principle applies to the other uncertainties. Representative cross-section together with their uncertainties are shown in Figures 4–6. The top-quark and top anti-quark t-channel production cross-sections, their combined values, and the ratio R_t, computed using various PDF sets, show a spread that is not fully consistent within PDF uncertainties for all sets. While some PDF sets, such as NNPDF3.0 and ATLAS epWZ16, yield similar cross-sections and R_t values, others, like ATLAS epWZVjet20 or ATLASpdf21, exhibit differences exceeding the combined PDF uncertainties. Overall, the different PDFs agree best for R_t where only ABM16 lies outside the PDF uncertainty band.
The cross-section increases by approximately 8.4% from 214.2 pb at 13 TeV to 232.2 pb at 13.6 TeV, reflecting the expected enhancement in cross-section due to higher collision energy. Due to differences in quark dynamics in the proton as described by the PDFs, R_t decreases at higher collision energy.

Table 4: The top-quark t-channel production cross-sections for $\sqrt{s}$ = 5.02 TeV in pb computed with MCFM and using different PDF sets, together with the uncertainties from scale, PDF and α_s variations, given as absolute uncertainties.

PDF set	$\sigma(tq)$ [pb]	scale unc.	PDF unc.	α_s unc.	Total unc.
ABM16 (5 flav.)	20.9	+0.3/-0.3	+0.1/-0.3	+0.2/-0.2	+0.4/-0.5
ATLAS epWZ16	20.7	+0.3/-0.2	+0.7/-0.8	+0.3/-0.3	+0.8/-0.8
ATLAS epWZtop18	20.8	+0.3/-0.2	+1.0/-0.6	+0.2/-0.1	+1.1/-0.7
ATLAS epWZVjet20	22.3	+0.3/-0.2	+0.3/-0.3	+0.1/-0.1	+0.4/-0.4
ATLASpdf21	22.5	+0.3/-0.2	+0.5/-0.4	-	+0.6/-0.5
CT18	20.4	+0.3/-0.2	+0.4/-0.4	+0.2/-0.2	+0.5/-0.5
MSHT2020	20.2	+0.3/-0.2	+0.1/-0.1	+0.2/-0.2	+0.4/-0.3
NNPDF3.0	21.2	+0.3/-0.2	+0.2/-0.2	+0.2/-0.1	+0.4/-0.3
NNPDF3.1	19.9	+0.3/-0.2	+0.1/-0.1	+0.3/-0.2	+0.4/-0.3
NNPDF4.0	19.7	+0.3/-0.2	+0.1/-0.1	+0.3/-0.3	+0.4/-0.3
PDF4LHC21	20.3	+0.3/-0.2	+0.1/-0.1	+0.3/-0.4	+0.4/-0.5

Table 5: The top anti-quark t-channel production cross-sections for $\sqrt{s}$ = 5.02 TeV in pb computed with MCFM and using different PDF sets, together with the uncertainties from renormalisation and factorisation scale, PDF and α_s variations, given as absolute uncertainties.

PDF set	$\sigma(\bar{t}q)$ [pb]	scale unc.	PDF unc.	α_s unc.	Total unc.
ABM16 (5 flav.)	9.4	+0.1/-0.1	+0.1/-0.1	+0.2/-0.1	+0.2/-0.2
ATLAS epWZ16	10.1	+0.2/-0.1	+0.4/-0.4	+0.2/-0.2	+0.5/-0.5
ATLAS epWZtop18	10.4	+0.2/-0.1	+0.5/-0.4	+0.1/-0.1	+0.6/-0.4
ATLAS epWZVjet20	11.1	+0.2/-0.1	+0.2/-0.2	+0.1/-0.1	+0.2/-0.2
ATLASpdf21	11.5	+0.2/-0.1	+0.3/-0.3	-	+0.4/-0.3
CT18	9.9	+0.1/-0.1	+0.2/-0.2	+0.1/-0.1	+0.3/-0.2
MSHT2020	9.9	+0.1/-0.1	+0.1/-0.1	+0.1/-0.1	+0.2/-0.2
NNPDF3.0	10.7	+0.1/-0.1	+0.1/-0.1	+0.2/-0.2	+0.3/-0.3
NNPDF3.1	9.6	+0.1/-0.1	+0.1/-0.1	+0.1/-0.2	+0.2/-0.2
NNPDF4.0	9.7	+0.1/-0.1	+0.1/-0.1	+0.1/-0.2	+0.2/-0.2
PDF4LHC21	10.0	+0.1/-0.1	+0.1/-0.1	+0.2/-0.1	+0.3/-0.2

Table 6: Prediction values obtained from MCFM for R_t for $\sqrt{s}$ = 5.02 TeV using different PDF sets as input, together with the uncertainties from renormalisation and factorisation scale, PDF and α_s variations and given as absolute uncertainties.

PDF set	R_t	scale unc.	PDF unc.	α_s unc.	Total unc.
ABMP16 (5 flav.)	2.23	+0.001/-0.002	+0.014/-0.015	+0.023/-0.008	+0.027/-0.017
ATLAS (epWZ16)	2.05	+0.001/-0.001	+0.029/-0.03	+0.009/-0.009	+0.03/-0.031
ATLAS (epWZtop18)	2.01	+0.001/-0.001	+0.014/-0.015	+0.003/-0.003	+0.015/-0.015
ATLAS (epWZVjet20)	2.02	+0.001/-0.001	+0.021/-0.021	+0.003 /-0.003	+0.022/-0.022
ATLASpdf21	1.95	+0.001/-0.001	+0.047/-0.047	-	+0.047/-0.047
CT18	2.07	+0.001/-0.001	+0.054/-0.064	+0.002/-0.011	+0.054/-0.065
MSHT2020	2.03	+0.001/-0.001	+0.024/-0.023	+0.004/-0.004	+0.025/-0.023
NNPDF 3.0	2.00	+0.001/-0.001	+0.031/-0.031	+0.016/-0.027	+0.035/-0.041
NNPDF 3.1	2.07	+0.001/-0.001	+0.022/-0.022	+0.003/-0.013	+0.023/-0.026
NNPDF 4.0	2.03	+0.001/-0.001	+0.006/-0.012	+0.005/-0.004	+0.008/-0.013
PDF4LHC21	2.03	+0.001/-0.001	+0.022/-0.027	+0.035/-0.039	+0.041/-0.047

Table 7: The combined top-quark and top anti-quark t-channel production cross-sections for $\sqrt{s}$ = 5.02 TeV in pb computed with MCFM and using different PDF sets, together with the uncertainties from renormalisation and factorisation scale, PDF and α_s variations, given as absolute uncertainties.

PDF set	$\sigma(tq + \bar{t}q)$ [pb]	scale unc.	PDF unc.	α_s unc.	Total unc.
ABMP16 (5 flav.)	30.3	+0.4/-0.4	+0.2/-0.4	+0.3/-0.4	+0.6/-0.7
ATLAS (epWZ16)	30.8	+0.5/-0.3	+1.2/-1.2	+0.5/-0.5	+1.3/-1.3
ATLAS (epWZtop18)	31.3	+0.5/-0.3	+1.5/-1.0	+0.3/-0.1	+1.6/-1.0
ATLAS (epWZVjet20)	33.4	+0.5/-0.3	+0.4/-0.4	+0.2/-0.2	+0.7/-0.5
ATLASpdf21	34.0	+0.5/-0.3	+0.7/-0.6	-	+0.9/-0.6
CT18	30.3	+0.4/-0.3	+0.4/-0.4	+0.4/-0.3	+0.7/-0.6
MSHT2020	30.1	+0.4/-0.3	+0.2/-0.1	+0.3/-0.3	+0.6/-0.4
NNPDF 3.0	31.9	+0.4/-0.3	+0.2/-0.3	+0.3/-0.3	+0.6/-0.5
NNPDF 3.1	29.5	+0.4/-0.3	+0.1/-0.1	+0.4/-0.4	+0.6/-0.4
NNPDF 4.0	29.3	+0.4/-0.3	+0.1/-0.1	+0.4/-0.4	+0.6/-0.5
PDF4LHC21	30.3	+0.4/-0.3	+0.2/-0.2	+0.2/-0.5	+0.5/-0.7

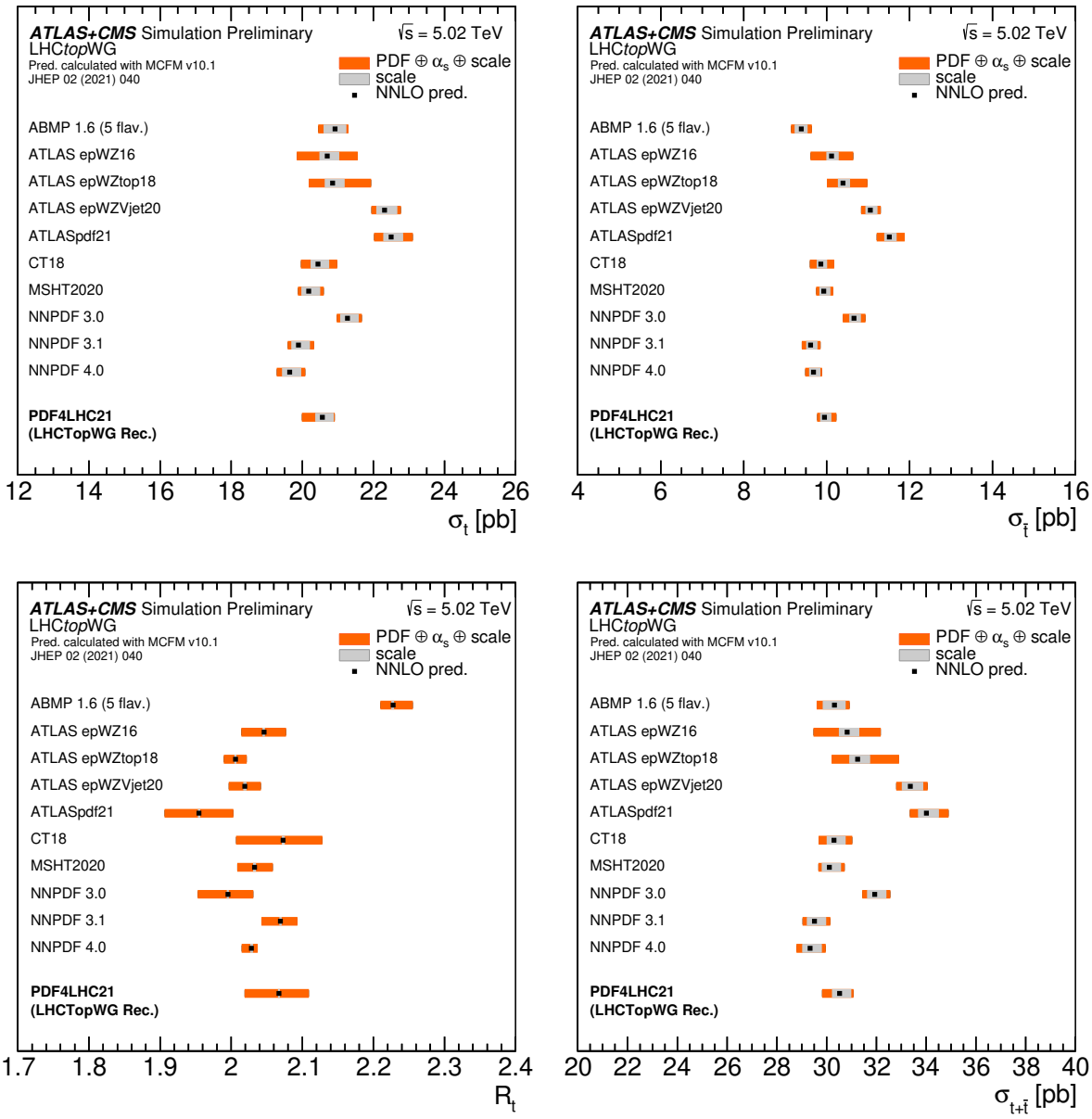

Figure 4: Values of $\sigma(tq)$ and $\sigma(\bar{t}q)$ in pb, R_t and $\sigma(tq+\bar{t}q)$ in pb calculated for different NNLO PDF sets for $\sqrt{s} = 5.02$ TeV. The uncertainty contains renormalisation and factorisation scale variations, PDF variations and the uncertainty on α_s.

Table 8: The top-quark t-channel production cross-sections for $\sqrt{s}$ = 13 TeV in pb computed with MCFM and using different PDF sets, together with the uncertainties from scale, PDF and α_s variations, given as absolute uncertainties.

PDF set	$\sigma(tq)$ [pb]	scale unc.	PDF unc.	α_s unc.	Total unc.
ABMP16 (5 flav.)	141.1	+1.5/-1.5	+1.2/-1.6	+1.6/-1.1	+1.9/-2.1
ATLAS (epWZ16)	138.8	+1.6/-1.0	+3.7/-3.5	+2.0/-1.6	+4.2/-3.9
ATLAS (epWZtop18)	139.6	+1.6/-1.1	+5.0/-3.3	+1.9/-1.1	+5.3/-3.5
ATLAS (epWZVjet20)	146.8	+1.7/-1.1	+2.3/-1.9	+1.8/-1.2	+2.9/-2.3
ATLASpdf21	147.0	+1.7/-1.2	+2.8/-2.3	-	+3.3/-2.6
CT18	134.1	+1.5/-1.1	+2.3/-2.5	+1.8/-1.5	+3.0/-3.0
MSHT2020	133.7	+1.5/-1.0	+1.6/-1.2	+2.1/-1.2	+2.6/-1.7
NNPDF 3.0	139.4	+1.5/-1.0	+1.5/-1.5	+0.5/-0.9	+2.1/-2.0
NNPDF 3.1	133.1	+1.5/-1.1	+1.7/-1.2	+1.9/-1.5	+2.5/-1.9
NNPDF 4.0	132.7	+1.5/-1.0	+1.5/-1.1	+2.3/-1.7	+2.7/-2.0
PDF4LHC21	134.2	+1.5/-1.1	+1.2/-1.2	+2.3/-1.2	+2.6/-1.7

Table 9: The top anti-quark t-channel production cross-sections for $\sqrt{s}$ = 13 TeV in pb computed with MCFM and using different PDF sets, together with the uncertainties from renormalisation and factorisation scale, PDF and α_s variations, given as absolute uncertainties.

PDF set	$\sigma(\bar{t}q)$ [pb]	scale unc.	PDF unc.	α_s unc.	Total unc.
ABMP16 (5 flav.)	79.2	+0.8/-0.8	+1.0/-1.0	+1.4/-0.6	+1.3/-1.3
ATLAS (epWZ16)	82.4	+0.9/-0.7	+2.5/-2.3	+1.3/-1.2	+2.8/-2.6
ATLAS (epWZtop18)	83.8	+1.0/-0.7	+3.3/-2.1	+1.2/-0.7	+3.5/-2.3
ATLAS (epWZVjet20)	87.7	+1.0/-0.7	+1.3/-1.1	+1.1/-0.8	+1.7/-1.4
ATLASpdf21	89.5	+1.0/-0.7	+1.9/-1.6	-	+2.1/-1.8
CT18	79.0	+0.9/-0.7	+1.2/-1.5	+1.2/-1.1	+1.8/-1.9
MSHT2020	79.9	+0.9/-0.7	+1.0/-0.8	+1.2/-1.1	+1.5/-1.4
NNPDF 3.0	84.2	+0.8/-0.7	+0.9/-0.9	+1.0/-1.3	+1.6/-1.7
NNPDF 3.1	78.7	+0.9/-0.7	+1.0/-0.8	+1.7/-1.0	+1.9/-1.2
NNPDF 4.0	79.1	+0.9/-0.7	+0.9/-0.7	+1.0/-1.0	+1.4/-1.2
PDF4LHC21	80.0	+0.8/-0.8	+1.1/-1.1	+1.2/-0.5	+1.8/-1.4

Table 10: Predicted values obtained from MCFM for R_t for $\sqrt{s}$ = 13 TeV using different PDF sets as input, together with the uncertainties from renormalisation and factorisation scale, PDF and α_s variations, given as absolute uncertainties.

PDF set	R_t	scale unc.	PDF unc.	α_s unc.	Total unc.
ABMP16 (5 flav.)	1.78	+0.012/-0.009	+0.011/-0.003	+0.027/-0.009	+0.044/-0.017
ATLAS (epWZ16)	1.68	+0.004/-0.002	+0.014/-0.014	+0.006/-0.005	+0.015/-0.015
ATLAS (epWZtop18)	1.67	+0.005/-0.002	+0.010/-0.007	+0.005/-0.002	+0.011/-0.008
ATLAS (epWZVjet20)	1.67	+0.007/-0.002	+0.015/-0.014	+0.007/-0.002	+0.017/-0.014
ATLASpdf21	1.64	+0.007/-0.002	+0.024/-0.024	-	+0.025/-0.024
CT18	1.70	+0.005/-0.001	+0.038/-0.035	+0.007/-0.005	+0.039/-0.035
MSHT2020	1.67	+0.003/-0.005	+0.015/-0.015	+0.004/-0.010	+0.016/-0.019
NNPDF 3.0	1.65	+0.001/-0.002	+0.024/-0.024	+0.013/-0.015	+0.027/-0.029
NNPDF 3.1	1.69	+0.003/-0.004	+0.012/-0.012	+0.018/-0.005	+0.021/-0.013
NNPDF 4.0	1.68	+0.002/-0.009	+0.004/-0.011	+0.011/-0.009	+0.011/-0.014
PDF4LHC21	1.68	+0.003/-0.002	+0.011/-0.014	+0.003/-0.002	+0.011/-0.015

Table 11: The combined top-quark and top anti-quark t-channel production cross-sections for $\sqrt{s}$ = 13 TeV in pb computed with MCFM and using different PDF sets, together with the uncertainties from renormalisation and factorisation scale, PDF and α_s variations, given as absolute uncertainties.

PDF set	$\sigma(tq+\bar{t}q)$ [pb]	scale unc.	PDF unc.	α_s unc.	Total unc.
ABMP16 (5 flav.)	220.3	+2.3/-2.3	+2.2/-2.5	+3.0/-1.5	+3.2/-3.4
ATLAS (epWZ16)	221.2	+2.5/-1.7	+5.8/-5.6	+2.6/-2.4	+6.9/-6.3
ATLAS (epWZtop18)	223.4	+2.6/-1.8	+8.1/-5.2	+2.3/-1.1	+8.9/-5.8
ATLAS (epWZVjet20)	234.5	+2.7/-1.8	+2.7/-2.4	+2.0/-1.5	+4.4/-4.5
ATLASpdf21	236.5	+2.7/-1.9	+4.4/-3.6	-	+5.1/-4.0
CT18	213.1	+2.4/-1.8	+2.3/-2.9	+2.4/-2.2	+4.3/-4.2
MSHT2020	213.6	+2.4/-1.6	+1.6/-1.2	+2.7/-1.8	+4.1/-2.9
NNPDF 3.0	223.6	+2.3/-1.7	+2.1/-2.1	+1.5/-2.2	+3.5/-3.5
NNPDF 3.1	211.8	+2.4/-1.7	+1.7/-1.3	+2.9/-2.1	+4.3/-3.1
NNPDF 4.0	211.8	+2.4/-1.7	+1.5/-1.1	+2.7/-2.3	+4.1/-3.2
PDF4LHC21	214.2	+2.4/-1.7	+1.6/-1.6	+2.9/-1.2	+4.1/-2.6

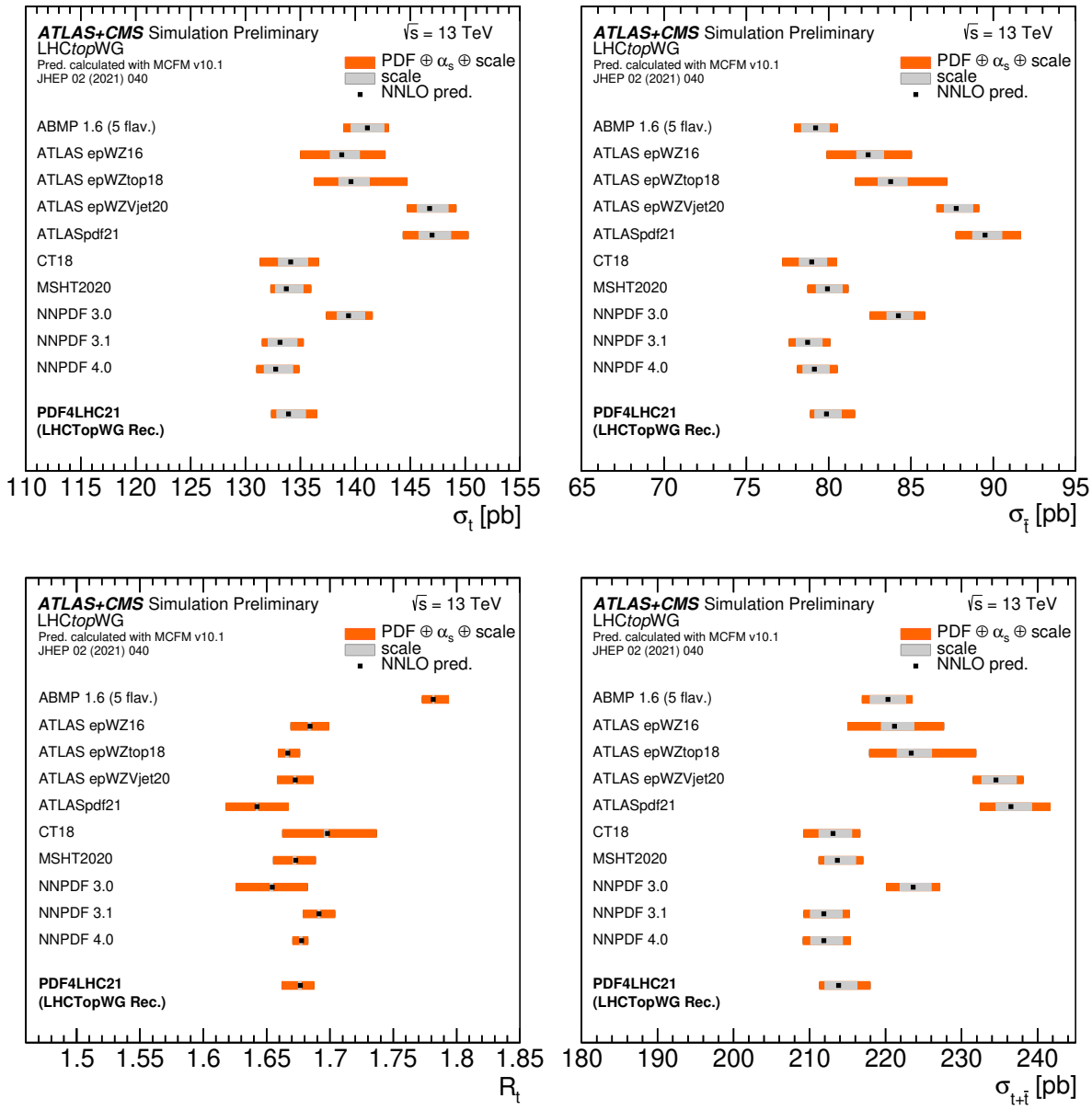

Figure 5: Values of $\sigma(tq)$ and $\sigma(\bar{t}q)$ in pb, R_t and $\sigma(tq + \bar{t}q)$ in pb calculated for different NNLO PDF sets for $\sqrt{s} = 13$ TeV. The uncertainty contains renormalisation and factorisation scale variations, PDF variations and the uncertainty on α_s.

Table 12: The top-quark t-channel production cross-sections for $\sqrt{s}$ = 13.6 TeV in pb computed using different PDF sets, together with the uncertainties from scale, PDF and α_s variations, given as absolute uncertainties.

PDF set	$\sigma(tq)$ [pb]	scale unc.	PDF unc.	α_s unc.	Total unc.
ABMP16 (5 flav.)	152.5	+1.6/-1.6	+0.3/-1.5	+1.5/-0.7	+2.3/-2.3
ATLAS (epWZ16)	150.0	+1.7/-1.2	+3.5/-3.8	+1.3/-1.3	+4.1/-4.1
ATLAS (epWZtop18)	151.3	+1.8/-1.2	+5.1/-3.7	+0.9/-0.1	+5.5/-3.9
ATLAS (epWZVjet20)	158.5	1.8/-1.3	+1.7/-1.7	+0.6/-0.61	+2.5/-2.2
ATLASpdf21	158.8	+1.8/-1.3	+2.9/-2.5	-	+3.5/-2.8
CT18	145.0	+1.6/-1.2	+1.7/-2.4	+0.9/-1.2	+2.5/-3.0
MSHT2020	144.8	+1.6/-1.1	+0.7/-0.7	+1.2/-1.3	+2.1/-1.9
NNPDF 3.0	150.6	+1.6/-1.2	+1.5/-1.5	+0.8/-0.5	+2.4/-2.1
NNPDF 3.1	144.2	+1.6/-1.1	+0.6/-0.6	+1.2/-1.2	+2.1/-1.8
NNPDF 4.0	143.6	+1.6/-1.1	+0.2/-0.3	+1.0/-1.6	+1.9/-2.0
PDF4LHC21	145.0	+1.6/-1.2	+0.7/-0.9	+1.4/-0.9	+2.3/-1.8

Table 13: The top anti-quark t-channel production cross-sections for $\sqrt{s}$ = 13.6 TeV in pb computed with MCFM and using different PDF sets, together with the uncertainties from renormalisation and factorisation scale, PDF and α_s variations, given as absolute uncertainties.

PDF set	$\sigma(\bar{t}q)$ [pb]	scale unc.	PDF unc.	α_s unc.	Total unc.
ABMP16 (5 flav.)	86.4	+0.9/-0.9	+0.3/-0.9	+0.7/-0.5	+1.2/-1.4
ATLAS (epWZ16)	89.6	+1.0/-0.8	+2.2/-2.6	+1.0/-1.0	+2.7/-2.9
ATLAS (epWZtop18)	91.3	+1.1/-0.9	+3.4/-2.0	+0.7/-0.1	+3.6/-2.2
ATLAS (epWZVjet20)	95.5	+1.1/-0.8	+0.9/-0.9	+0.5/-0.5	+1.5/-1.3
ATLASpdf21	97.3	+1.1/-0.8	+2.0/-1.7	-	+2.3/-1.9
CT18	86.0	+1.0/-0.8	+0.9/-1.3	+0.8/-0.7	+1.5/-1.7
MSHT2020	87.2	+1.0/-0.7	+0.5/-0.5	+0.5/-0.8	+1.2/-1.2
NNPDF 3.0	91.7	+1.0/-0.8	+0.9/-0.9	+1.0/-1.3	+1.7/-1.8
NNPDF 3.1	85.8	+1.0/-0.8	+0.4/-0.4	+1.0/-1.0	+1.5/-1.3
NNPDF 4.0	86.2	+1.0/-0.8	+0.2/-0.1	+1.1/-0.9	+1.5/-1.2
PDF4LHC21	87.2	+0.9/-0.7	+0.9/-0.6	+1.2/-0.7	+1.7/-1.2

Table 14: Predicted values obtained from MCFM for R_t for $\sqrt{s}$ = 13.6 TeV using different PDF sets as input, together with the uncertainties from renormalisation and factorisation scale, PDF and α_s variations and given as absolute uncertainties.

PDF set	R_t	scale unc.	PDF unc.	α_s unc.	Total unc.
ABMP16 (5 flav.)	1.76	+0.001/-0.001	+0.009/-0.008	+0.004/-0.003	+0.010/-0.009
ATLAS (epWZ16)	1.67	+0.001/-0.002	+0.014/-0.014	+0.004/-0.004	+0.015/-0.015
ATLAS (epWZtop18)	1.65	+0.001/-0.002	+0.013/-0.014	+0.002/-0.001	+0.013/-0.014
ATLAS (epWZVjet20)	1.65	+0.001/-0.001	+0.013/-0.013	+0.002/-0.002	+0.014/-0.014
ATLASpdf21	1.63	+0.001/-0.001	+0.024/-0.024	-	+0.024/-0.024
CT18	1.68	+0.001/-0.001	+0.033/-0.034	+0.004/-0.001	+0.033/-0.034
MSHT2020	1.65	+0.001/-0.001	+0.015/-0.014	+0.004/-0.001	+0.015/-0.015
NNPDF 3.0	1.64	+0.001/-0.001	+0.024/-0.024	+0.009/-0.017	+0.026/-0.029
NNPDF 3.1	1.67	+0.001/-0.002	+0.011/-0.011	+0.005/-0.004	+0.012/-0.012
NNPDF 4.0	1.66	+0.001/-0.002	+0.003/-0.006	+0.009/-0.003	+0.010/-0.007
PDF4LHC21	1.66	+0.001/-0.001	+0.010/-0.014	+0.006/-0.002	+0.012/-0.014

Table 15: The combined top-quark and top anti-quark t-channel production cross-sections for $\sqrt{s}$ = 13.6 TeV in pb computed with MCFM and using different PDF sets, together with the uncertainties from renormalisation and factorisation scale, PDF and α_s variations a, given as absolute uncertainties.

PDF set	$\sigma(tq + \bar{t}q)$ [pb]	scale unc.	PDF unc.	α_s unc.	Total unc.
ABMP16 (5 flav.)	238.9	+2.6/-2.5	+0.5/-2.4	+2.2/-1.2	+3.4/-3.7
ATLAS (epWZ16)	239.5	+2.8/-2.0	+5.6/6.2	+2.2/-2.3	+6.6/-6.9
ATLAS (epWZtop18)	242.5	+2.9/-2.1	+8.5/-5.7	+1.7/-0.2	+9.1/-6.1
ATLAS (epWZVjet20)	253.9	+2.9/-2.1	+2.3/-2.3	+1.1/-1.1	+3.9/-3.3
ATLASpdf21	256.1	+2.9/-2.1	+4.7/-3.8	-	+5.5/-4.4
CT18	231.1	+2.6/-2.0	1.8 -3.0	+1.7/-2.0	+3.6/-4.1
MSHT2020	231.9	+2.6/-1.9	+0.7/-0.8	+1.8/-2.2	+3.2/-3.0
NNPDF 3.0	242.3	+2.6/-2.0	+2.3/-2.3	+1.9/-1.9	+3.9/-3.6
NNPDF 3.1	230.0	+2.6/-2.0	+0.7/-0.7	+2.3/-2.2	+3.5/-3.0
NNPDF 4.0	229.8	+2.6/-2.0	+0.3/-0.3	+2.2/-2.6	+3.5/-3.2
PDF4LHC21	232.2	+2.6/-2.0	+1.4/-1.4	+2.7/-1.6	+4.0/-2.9

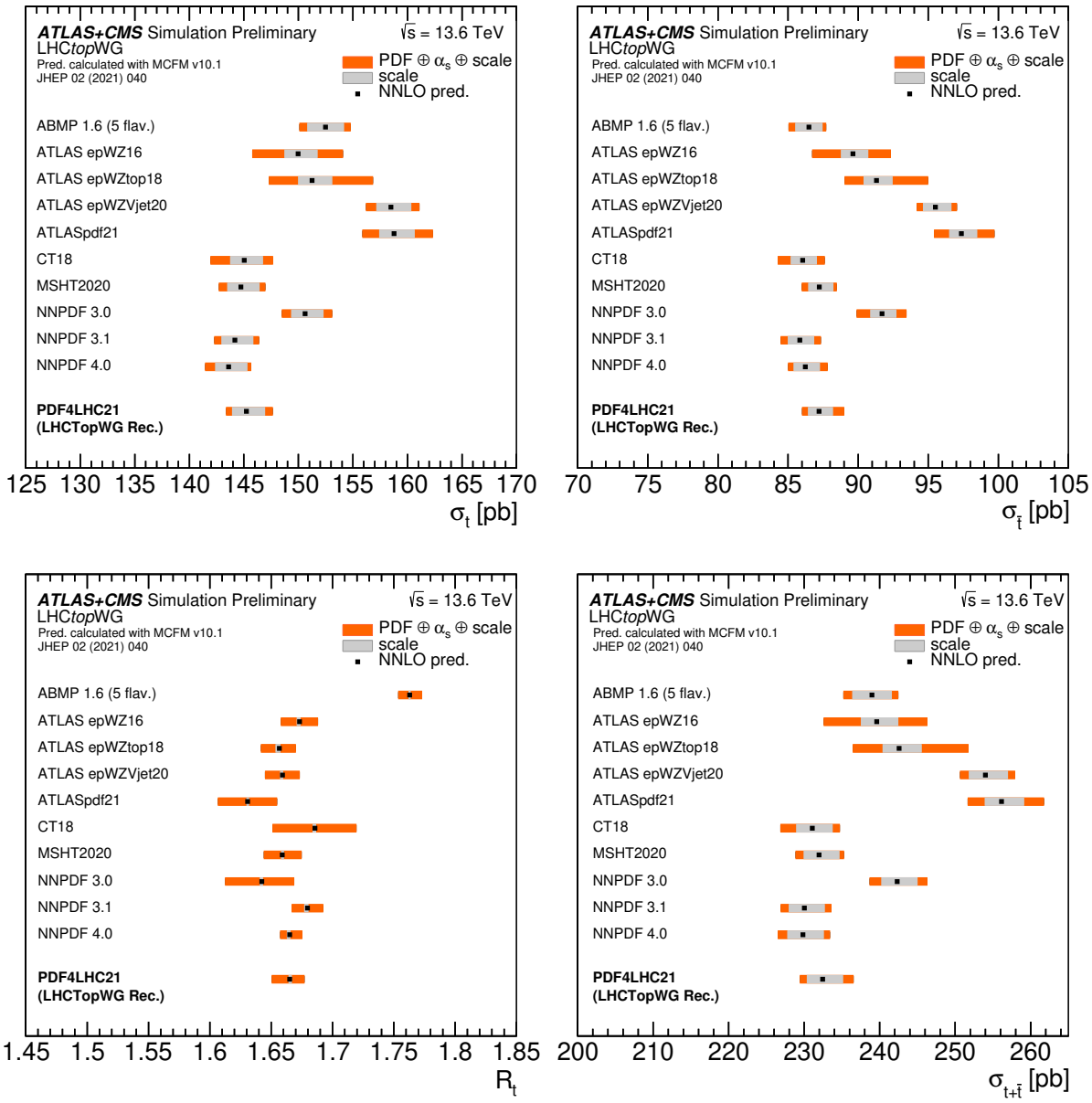

Figure 6: Values of $\sigma(tq)$ and $\sigma(\bar{t}q)$ in pb, R_t and $\sigma(tq + \bar{t}q)$ in pb calculated for different NNLO PDF sets for $\sqrt{s} = 13.6$ TeV. The uncertainty contains renormalisation and factorisation scale variations, PDF variations and the uncertainty on α_s.

3.1.2 Comparison between NLO and NNLO results

A detailed comparison between MCFM and Hathor at NLO is provided in Tables 16–19. Hathor uses a fixed scale of $\mu_r = \mu_f = m_{\text{top}}$, while MCFM defaults to a dynamic scale based on the DDIS choice. As a result, differences between the two calculations are more pronounced. However, these differences are significantly reduced when MCFM is configured to use the same fixed scale. It is also observed that most recent ATLAS PDF set ATLASpdf21 tend to predict higher cross-section values compared to all other PDF sets. This is most likely due to differences in the input datasets used in the PDF fits. All studies for Hathor and MCFM are performed at a CME of $\sqrt{s} = 13$ TeV.

Table 16: Comparison between Hathor and MCFM with NLO calculations and MCFM NNLO-calculations for σ_t. All values are in pb at $\sqrt{s} = 13$ TeV and the absolute uncertainty on the scale variation is given.

PDF set	Hathor NLO	MCFM NLO	MCFM NNLO	MCFM NLO DDIS
Scale	$\mu = m_{top}$	$\mu = m_{top}$	$\mu = m_{top}$	DDIS
ABMP16 (5 flav.)	$145.3^{+4.0}_{-4.0}$	$145.1^{+4.0}_{-2.9}$	$141.1^{+1.5}_{-1.5}$	$145.9^{+4.2}_{-3.1}$
ATLAS (epWZ16)	$143.4^{+4.1}_{-4.1}$	$142.9^{+4.1}_{-3.1}$	$138.8^{+1.6}_{-1.0}$	$143.8^{+4.4}_{-2.6}$
ATLAS (epWZtop18)	$144.3^{+4.2}_{-4.2}$	$144.0^{+4.2}_{-3.1}$	$139.6^{+1.6}_{-1.1}$	$144.9^{+4.4}_{-2.7}$
ATLAS (epWZVjet20)	$151.6^{+4.4}_{-4.4}$	$151.3^{+4.4}_{-3.3}$	$146.8^{+1.7}_{-1.1}$	$152.1^{+4.6}_{-2.7}$
ATLASpdf21	$151.8^{+4.2}_{-4.2}$	$151.5^{+4.2}_{-3.2}$	$147.0^{+1.7}_{-1.2}$	$152.2^{+4.5}_{-2.7}$
CT18	$138.7^{+4.1}_{-4.1}$	$138.4^{+4.1}_{-3.0}$	$134.1^{+1.5}_{-1.1}$	$139.1^{+4.3}_{-2.5}$
MSHT2020	$138.4^{+5.1}_{-4.1}$	$138.1^{+4.1}_{-3.0}$	$133.7^{+1.5}_{-1.0}$	$138.8^{+4.2}_{-2.5}$
NNPDF 3.1	$137.2^{+4.1}_{-4.1}$	$137.5^{+4.1}_{-3.0}$	$133.1^{+1.5}_{-1.1}$	$138.2^{+4.3}_{-2.5}$
NNPDF 4.0	$137.2^{+4.1}_{-4.1}$	$136.9^{+4.1}_{-3.0}$	$132.7^{+1.5}_{-1.0}$	$137.7^{+4.3}_{-2.5}$
PDF4LHC21	$138.6^{+4.1}_{-4.1}$	$138.3^{+4.1}_{-3.0}$	$134.2^{+1.5}_{-1.1}$	$139.1^{+4.2}_{-2.5}$

Table 17: Comparison between Hathor and MCFM with NLO calculations and MCFM NNLO-calculations for $\sigma_{\bar{t}}$. All values are in pb at $\sqrt{s} = 13$ TeV and the absolute uncertainty on the scale variation is given.

PDF set	Hathor NLO	MCFM NLO	MCFM NNLO	MCFM NLO DDIS
Scale	$\mu = m_{top}$	$\mu = m_{top}$	$\mu = m_{top}$	DDIS
ABMP16 (5 flav.)	$82.4^{+2.3}_{-2.3}$	$82.3^{+2.3}_{-1.6}$	$79.2^{+0.8}_{-0.8}$	$82.2^{+2.3}_{-1.7}$
ATLAS (epWZ16)	$85.8^{+2.5}_{-2.5}$	$85.6^{+2.5}_{-1.8}$	$82.4^{+0.9}_{-0.7}$	$85.6^{+2.6}_{-1.5}$
ATLAS (epWZtop18)	$87.3^{+2.5}_{-2.5}$	$87.1^{+2.6}_{-1.8}$	$83.8^{+1.0}_{-0.7}$	$87.1^{+2.6}_{-1.5}$
ATLAS (epWZVjet20)	$91.2^{+2.7}_{-2.7}$	$91.1^{+2.7}_{-1.9}$	$87.7^{+1.0}_{-0.7}$	$91.0^{+2.7}_{-1.6}$
ATLASpdf21	$93.1^{+2.7}_{-2.7}$	$93.0^{+2.7}_{-1.9}$	$89.5^{+1.0}_{-0.7}$	$92.9^{+2.7}_{-1.6}$
CT18	$82.4^{+2.5}_{-2.5}$	$82.3^{+2.5}_{-1.7}$	$79.0^{+0.9}_{-0.7}$	$82.2^{+2.5}_{-1.4}$
MSHT2020	$83.3^{+2.5}_{-2.5}$	$83.1^{+2.5}_{-1.7}$	$79.9^{+0.9}_{-0.7}$	$83.1^{+2.5}_{-1.4}$
NNPDF 3.1	$81.7^{+2.5}_{-2.5}$	$81.9^{+2.5}_{-1.7}$	$78.7^{+0.9}_{-0.7}$	$81.9^{+2.5}_{-1.4}$
NNPDF 4.0	$82.5^{+2.5}_{-2.5}$	$82.3^{+2.5}_{-1.7}$	$79.1^{+0.9}_{-0.7}$	$82.3^{+2.5}_{-1.4}$
PDF4LHC21	$83.3^{+2.5}_{-2.5}$	$83.2^{+2.5}_{-1.1}$	$80.0^{+0.8}_{-0.8}$	$83.1^{+2.5}_{-1.4}$

Table 18: Comparison between HATHOR and MCFM with NLO calculations and MCFM NNLO-calculations for R_t. All values are in pb at $\sqrt{s} = 13$ TeV and the absolute uncertainty on the scale variation is given.

PDF set	HATHOR NLO	MCFM NLO	MCFM NNLO	MCFM NLO DDIS
Scale	$\mu = m_{top}$	$\mu = m_{top}$	$\mu = m_{top}$	DDIS
ABMP16 (5 flav.)	$1.76^{+0.005}_{-0.003}$	$1.76^{+0.002}_{-0.001}$	$1.78^{+0.024}_{-0.002}$	$1.77^{+0.002}_{-0.002}$
ATLAS (epWZ16)	$1.67^{+0.004}_{-0.003}$	$1.67^{+0.002}_{-0.002}$	$1.68^{+0.004}_{-0.002}$	$1.68^{+0.002}_{-0.002}$
ATLAS (epWZtop18)	$1.65^{+0.004}_{-0.003}$	$1.65^{+0.002}_{-0.002}$	$1.67^{+0.005}_{-0.002}$	$1.66^{+0.002}_{-0.002}$
ATLAS (epWZVjet20)	$1.66^{+0.005}_{-0.002}$	$1.66^{+0.002}_{-0.001}$	$1.67^{+0.007}_{-0.002}$	$1.67^{+0.002}_{-0.002}$
ATLASpdf21	$1.63^{+0.005}_{-0.002}$	$1.63^{+0.002}_{-0.001}$	$1.64^{+0.007}_{-0.002}$	$1.64^{+0.002}_{-0.002}$
CT18	$1.68^{+0.006}_{-0.003}$	$1.68^{+0.002}_{-0.001}$	$1.70^{+0.005}_{-0.001}$	$1.69^{+0.002}_{-0.002}$
MSHT2020	$1.66^{+0.005}_{-0.002}$	$1.66^{+0.002}_{-0.001}$	$1.67^{+0.003}_{-0.005}$	$1.67^{+0.002}_{-0.002}$
NNPDF 3.1	$1.68^{+0.006}_{-0.002}$	$1.68^{+0.002}_{-0.001}$	$1.69^{+0.003}_{-0.004}$	$1.69^{+0.002}_{-0.002}$
NNPDF 4.0	$1.66^{+0.005}_{-0.003}$	$1.66^{+0.002}_{-0.002}$	$1.68^{+0.002}_{-0.009}$	$1.67^{+0.002}_{-0.002}$
PDF4LHC21	$1.66^{+0.005}_{-0.003}$	$1.66^{+0.002}_{-0.001}$	$1.68^{+0.003}_{-0.002}$	$1.67^{+0.002}_{-0.002}$

Table 19: Comparison between HATHOR and MCFM with NLO calculations and MCFM NNLO-calculations for $\sigma_{t+\bar{t}}$. All values are in pb at $\sqrt{s} = 13$ TeV and the absolute uncertainty on the scale variation is given.

PDF set	HATHOR NLO	MCFM NLO	MCFM NNLO	MCFM NLO DDIS
Scale	$\mu = m_{top}$	$\mu = m_{top}$	$\mu = m_{top}$	DDIS
ABMP16 (5 flav.)	$227.7^{+6.3}_{-6.3}$	$227.4^{+6.3}_{-4.4}$	$220.3^{+2.3}_{-2.3}$	$228.1^{+6.5}_{-4.8}$
ATLAS (epWZ16)	$229.2^{+6.7}_{-6.7}$	$228.5^{+6.6}_{-4.8}$	$221.2^{+2.5}_{-1.7}$	$229.4^{+6.9}_{-4.8}$
ATLAS (epWZtop18)	$231.6^{+6.7}_{-6.7}$	$231.1^{+6.7}_{-4.9}$	$223.4^{+2.6}_{-1.8}$	$232.0^{+7.0}_{-4.2}$
ATLAS (epWZVjet20)	$242.8^{+7.0}_{-7.0}$	$242.4^{+7.1}_{-5.2}$	$234.5^{+2.7}_{-1.8}$	$243.1^{+7.3}_{-4.3}$
ATLASpdf21	$244.9^{+6.9}_{-6.9}$	$244.5^{+6.9}_{-5.0}$	$236.5^{+2.7}_{-1.9}$	$245.1^{+7.1}_{-4.2}$
CT18	$221.1^{+6.5}_{-6.5}$	$220.7^{+6.5}_{-4.7}$	$213.1^{+2.4}_{-1.8}$	$221.3^{+6.7}_{-3.9}$
MSHT2020	$221.7^{+6.5}_{-6.5}$	$221.2^{+6.5}_{-4.7}$	$213.6^{+2.4}_{-1.6}$	$221.9^{+6.8}_{-3.9}$
NNPDF 3.1	$218.9^{+6.7}_{-6.7}$	$219.4^{+6.6}_{-4.7}$	$211.8^{+2.4}_{-1.7}$	$220.1^{+6.8}_{-3.9}$
NNPDF 4.0	$219.7^{+6.6}_{-6.6}$	$219.2^{+6.6}_{-4.7}$	$211.8^{+2.4}_{-1.7}$	$220.0^{+6.8}_{-3.9}$
PDF4LHC21	$221.9^{+6.5}_{-6.5}$	$221.5^{+6.5}_{-4.7}$	$214.2^{+2.4}_{-1.7}$	$222.2^{+6.8}_{-3.9}$

3.2 LHC Top WG recommendation

In Table 20, the definitions and settings used for the scale, the nominal PDF, and m_{top}, together with their corresponding uncertainties, are presented. The recommended cross-sections are given in Table 21, with uncertainties including contributions from the scale, PDF+α_s, m_{top}, and E_{beam}. For most analyses it is recommended to add the scale and PDF+α_s uncertainties together and quote them as the total uncertainty. Analyses such as searches or precision measurements can also add the m_{top} and E_{Beam} terms in quadrature. Additionally, the numerical uncertainty due to the integration procedure implemented in MCFM is quoted. Results for the parametrisation of m_{top} and $\sqrt{s}$ can be found in Table 23 and Table 22. The energy parametrisation for $\sigma(t)$, $\sigma(\bar{t})$ and R_t are also shown in Figure 7. Values indicated with < 0.1 can be ignored for practical purposes.

Table 20: Summary of the settings for the t-channel singl top-quark production recommendations.

Setting	Value	Uncertainty Definition
Scale	DDIS	7 point envelope
PDF	PDF4LHC21	Hessian approach
Top-Quark Mass (m_{top})	172.5 GeV	$\pm$1.0 GeV

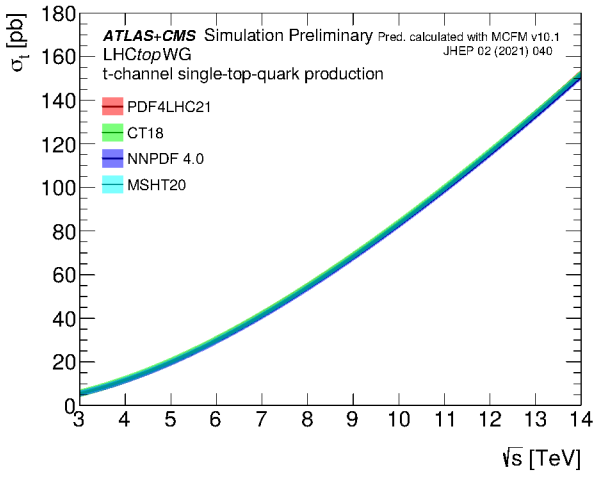

(a) Top-quark production

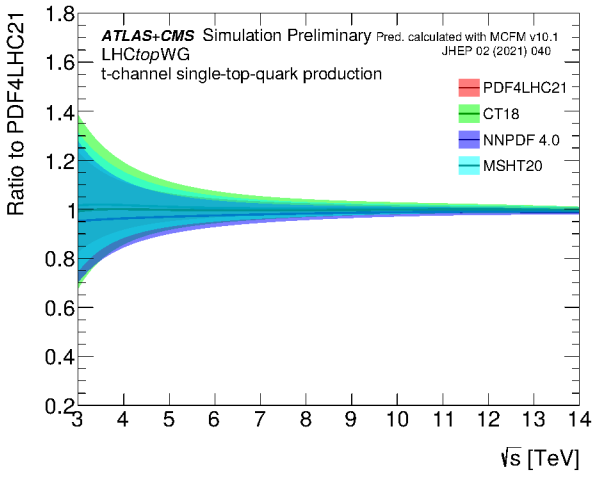

(b) Top-quark production

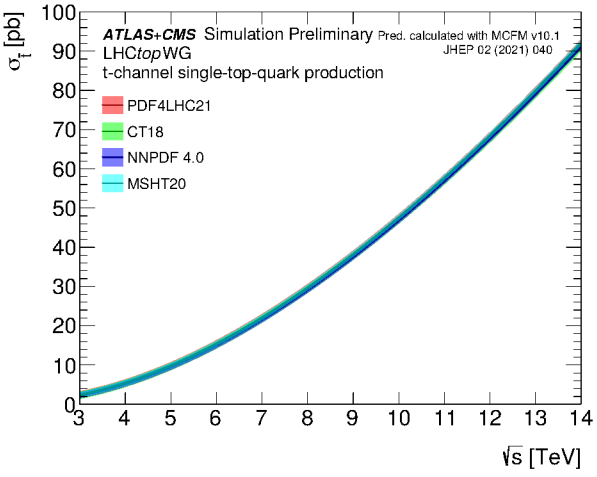

(c) Top-antiquark production

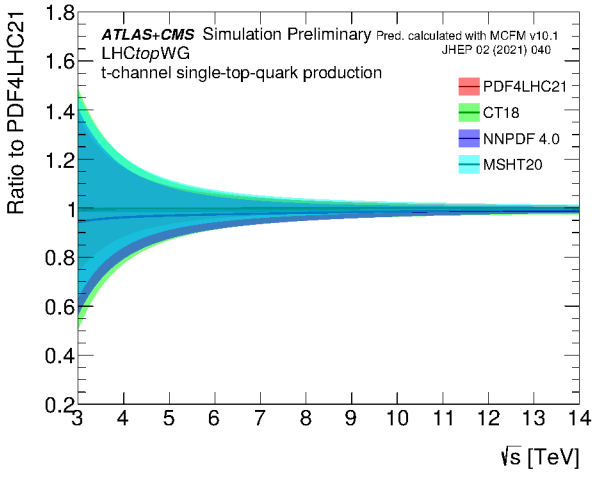

(d) Top-antiquark production

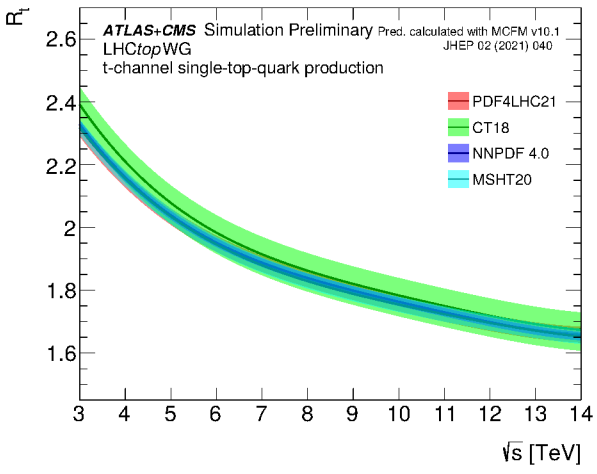

(e) R_t

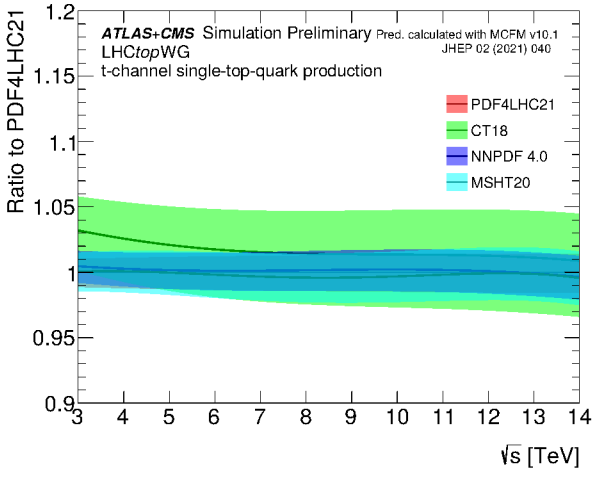

(f) R_t

Figure 7: Parametrisation for the energy dependence of the t-channel production cross-section for (a) top-quark production, (c) top-antiquark production, (e) R_t and the ratio to PDF4LHC21 for (b) top-quark production, (d) top-antiquark production, (f) R_t.

Table 21: Predicted values obtained from MCFM for $\sigma(tq)$, $\sigma(\bar{t}q)$ and $\sigma(tq+\bar{t}q)$ in pb using the PDF4LHC21 PDF set as input, together with the uncertainties from scale, PDF, α_s, m_{top} and beam-energy variations. The total uncertainty is given by adding scale and PDF uncertainties in quadrature.

Mode	Central value	Scale	PDF $\oplus$ α_s	Total	m_{top}	E_{beam}	Integration
$\sigma(tq)$	20.3	+0.3/-0.2	+0.4/-0.3	+0.5/-0.4	+0.1/-0.2	<0.1	<0.1
$\sigma(\bar{t}q)$	10.0	+0.1/-0.1	+0.3/-0.2	+0.2/-0.3	+0.1/-0.1	<0.1	<0.1
$\sigma(tq+\bar{t}q)$	30.3	+0.4/-0.3	+0.6/-0.4	+0.7/-0.5	+0.2/-0.3	+0.1/-0.1	<0.1

(a) 5.02 TeV

Mode	Central value	Scale	PDF $\oplus$ α_s	Total	m_{top}	E_{beam}	Integration
$\sigma(tq)$	41.7	+0.6/-0.3	+0.7/-0.5	+0.9/-0.6	+0.4/-0.4	+0.1/-0.1	<0.1
$\sigma(\bar{t}q)$	22.1	+0.3/-0.2	+0.5/-0.4	+0.6/-0.4	+0.2/-0.2	+0.1/-0.1	<0.1
$\sigma(tq+\bar{t}q)$	63.7	+0.9/-0.5	+1.1/-0.7	+1.4/-0.8	+0.6/-0.6	+0.2/-0.1	+0.1/-0.1

(b) 7 TeV

Mode	Central value	Scale	PDF $\oplus$ α_s	Total	m_{top}	E_{beam}	Integration
$\sigma(tq)$	54.6	+0.7/-0.4	+0.9/-0.7	+1.1/-0.8	+0.6/-0.4	+0.1/-0.2	+0.1/-0.1
$\sigma(\bar{t}q)$	29.7	+0.4/-0.3	+0.6/-0.5	+0.7/-0.6	+0.3/-0.3	+0.1/-0.1	<0.1
$\sigma(tq+\bar{t}q)$	84.3	+1.1/-0.7	+1.4/-0.9	+1.7/-1.2	+0.9/-0.7	+0.2/-0.2	+0.1/-0.1

(c) 8 TeV

Mode	Central value	Scale	PDF $\oplus$ α_s	Total	m_{top}	E_{beam}	Integration
$\sigma(tq)$	134.2	+1.5/-1.1	+2.1/-1.3	+2.6/-1.7	+1.2/-1.0	+0.2/-0.2	+0.1/-0.1
$\sigma(\bar{t}q)$	80.0	+0.8/-0.8	+1.6/-1.2	+1.8/-1.4	+0.7/-0.7	+0.1/-0.2	+0.1/-0.1
$\sigma(tq+\bar{t}q)$	214.2	+2.4/-1.7	+3.3/-2.0	+4.1/-2.6	+1.9/-1.7	+0.3/-0.4	+0.2/-0.2

(d) 13 TeV

Mode	Central value	Scale	PDF $\oplus$ α_s	Total	m_{top}	E_{beam}	Integration
$\sigma(tq)$	145.0	+1.7/-1.1	+2.3/-1.5	+2.8/-1.9	+0.9/-1.3	+0.3/-0.4	+0.1/-0.1
$\sigma(\bar{t}q)$	87.2	+0.9/-0.8	+1.5/-1.3	+1.8/-1.5	+0.7/-0.6	+0.2/-0.2	+0.1/-0.1
$\sigma(tq+\bar{t}q)$	232.2	+2.6/-1.9	+3.4/-2.2	+4.3/-2.9	+1.6/-1.9	+0.5/-0.6	+0.2/-0.2

(e) 13.6 TeV

Mode	Central value	Scale	PDF $\oplus$ α_s	Total	m_{top}	E_{beam}	Integration
$\sigma(tq)$	152.4	+1.7/-1.2	+2.2/-1.8	+2.8/-2.4	+1.3/-1.3	+0.2/-0.4	+0.1/-0.1
$\sigma(\bar{t}q)$	92.1	+1.0/-0.8	+1.7/-1.3	+2.0/-1.5	+0.8/-0.7	+0.1/-0.2	+0.1/-0.1
$\sigma(tq+\bar{t}q)$	244.5	+2.7/-2.0	+3.5/-2.5	+4.4/-3.1	+2.1/-1.9	+0.3/-0.6	+0.2/-0.2

(f) 14 TeV

Table 22: Mass parametrizations for the top- and antitop- t-channel production cross-sections for different center-of-mass energies.

Mode	a_0	a_1
$\sigma(tq)$	2.206	0.285
$\sigma(\bar{t}q)$	2.054	0.079
$\sigma(tq+\bar{t}q)$	2.156	0.155

(a) 5.02 TeV

Mode	a_0	a_1
$\sigma(tq)$	2.457	0.011
$\sigma(\bar{t}q)$	2.277	0.259
$\sigma(tq+\bar{t}q)$	2.398	0.010

(b) 7 TeV

Mode	a_0	a_1
$\sigma(tq)$	2.394	15.072
$\sigma(\bar{t}q)$	2.328	12.385
$\sigma(tq+\bar{t}q)$	2.371	13.947

(c) 8 TeV

Mode	a_0	a_1
$\sigma(tq)$	2.619	0.032
$\sigma(\bar{t}q)$	2.482	9.523
$\sigma(tq+\bar{t}q)$	2.569	0.141

(d) 13 TeV

Mode	a_0	a_1
$\sigma(tq)$	3.599	21.975
$\sigma(\bar{t}q)$	3.584	0.052
$\sigma(tq+\bar{t}q)$	3.591	11.106

(e) 13.6 TeV

Mode	a_0	a_1
$\sigma(tq)$	2.572	0.533
$\sigma(\bar{t}q)$	2.641	0.035
$\sigma(tq+\bar{t}q)$	2.599	0.190

(f) 14 TeV

Table 23: Energy parametrisation for the top-quark and top-antiquark t-channel production cross-sections. The coefficients a_i ($i \in \{0, ..., 6\}$) represent the free parameters from the energy-parametrisation in Eq. (4)

Mode	a_0	a_1	a_2	a_3	a_4	a_5	a_6
$\sigma(tq)$	-0.759	-5.094	1.146	2.158	0.95	-0.739	0.176
$\sigma(\bar{t}q)$	-0.678	-2.902	0.682	0.395	0.091	-0.271	0.092
$\sigma(tq+\bar{t}q)$	-3.937	-11.926	2.119	0.014	1.171	-1.168	0.162

.

3.3 Prediction of differential cross-sections

In addition to the inclusive cross-sections, predictions for the p_{T} and rapidity of the top quark in the t-channel single top-quark production for $\sqrt{\hat{s}} = 13$ TeV are shown in Figure 8 for NNLO, in Figure 9 for LO, NLO and NNLO and in Figure 10 for a fixed renormalisation and factorisation scale and the DDIS scale. While the differences due to the choice of scales are only visible in the high-p_{T} tail, the differences between LO, NLO and NNLO are more visible. Notably, higher order corrections lead to negative interference and thus result in reduced cross-sections.

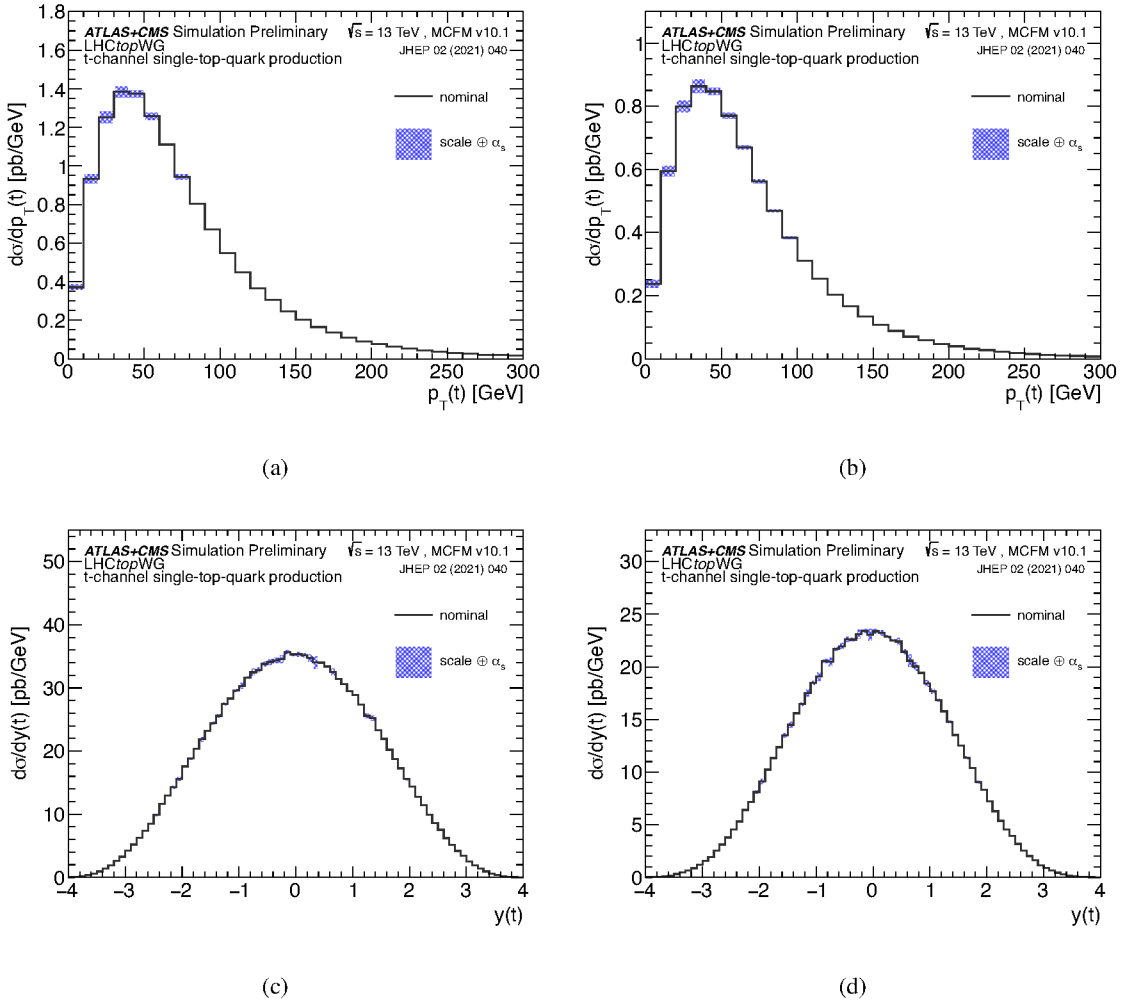

Figure 8: Predictions at NNLO obtained with MCFM of $p_{\mathrm{T}}(t)$ and $y(t)$ using the DDIS scale at $\sqrt{s} = 13$ TeV and PDF4LHC21. Figure 8(a) and Figure 8(b) show $p_{\mathrm{T}}(t)$ for top-quark and top-antiquark production respectively. Figure 8(c) and Figure 8(d) show $y(t)$ for top-quark and top-antiquark production respectively. The blue band represents the uncertainty on the renormalisation and factorisation scale choice and the value of α_{s} as well as the numerical uncertainty.

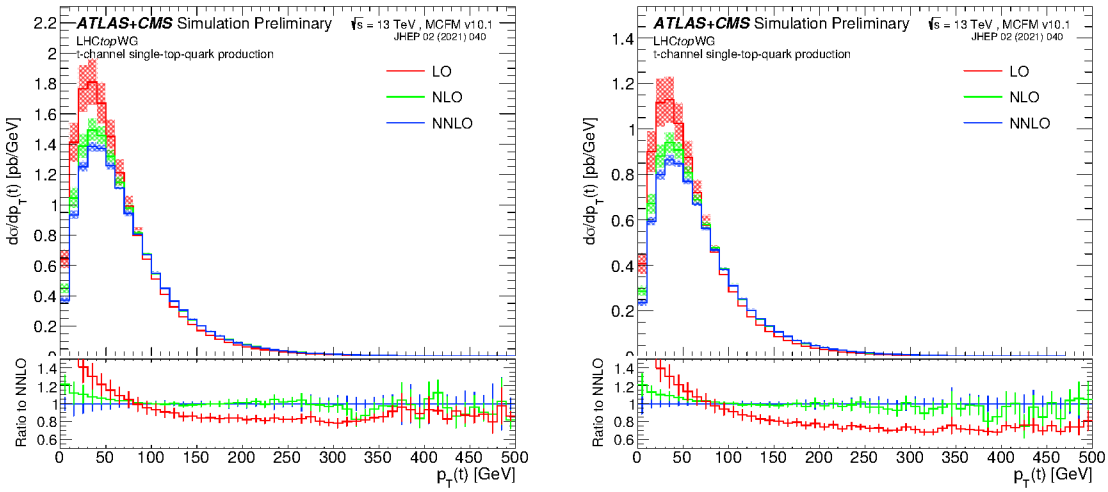

(a)

(b)

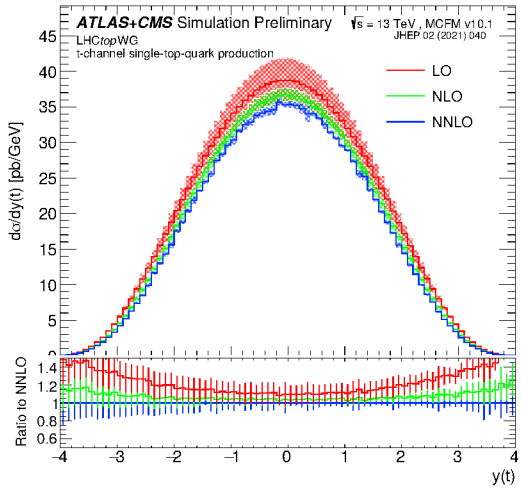

(c)

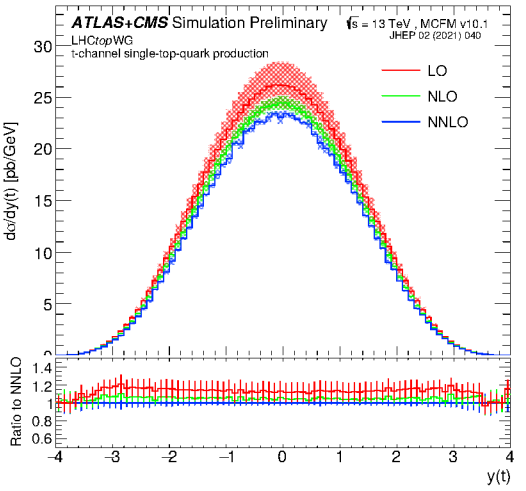

(d)

Figure 9: Predictions at LO, NLO and NNLO obtained with MCFM of $p_{\mathrm{T}}(t)$ and $y(t)$ using the DDIS scale at $\sqrt{s}$ = 13 TeV and PDF4LHC21. Figure 9(a) and Figure 9(b) show $p_{\mathrm{T}}(t)$ for top-quark and top-antiquark production respectively. Figure 9(c) and Figure 9(d) show $y(t)$ for top-quark and top-antiquark production respectively. The colored bands represent the uncertainty on the renormalisation and factorisation scale choice and the value of α_{s} as well as the numerical uncertainty.

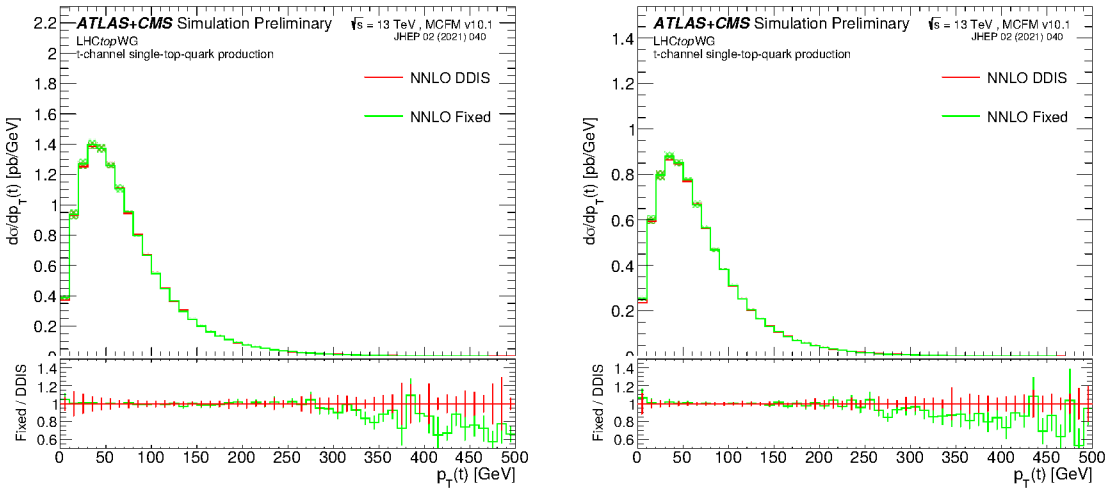

(a)

(b)

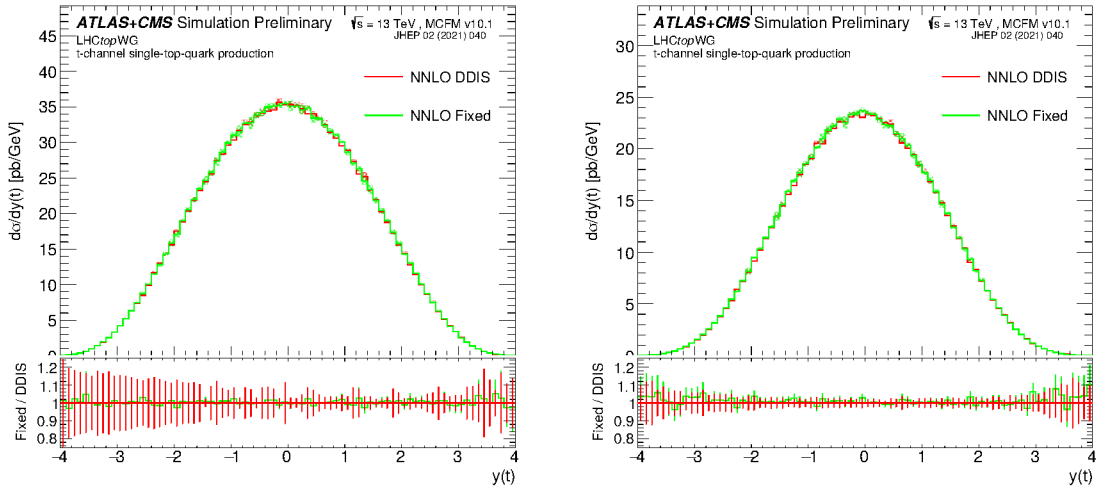

(c)

(d)

Figure 10: Predictions at NNLO obtained with MCFM of $p_{\mathrm{T}}(t)$ and $y(t)$ for a fixed scale of $\mu_r = \mu_f = m_{\mathrm{top}}$ and the DDIS scale at $\sqrt{s} = 13\,\mathrm{TeV}$ and PDF4LHC21. Figure 10(a) and Figure 10(b) show $p_{\mathrm{T}}(t)$ for top-quark and top-antiquark production respectively. Figure 10(c) and Figure 10(d) show $y(t)$ for top-quark and top-antiquark production respectively. The colored bands represent the uncertainty on the renormalisation and factorisation scale choice and the value of α_{s} as well as the numerical uncertainty.

4 tW associated production

This section presents results for associated tW production. An example LO Feynman diagram is shown in Figure 11. Details of the calculation of the inclusive cross-sections are given in Ref. [5]. Here, the cross-

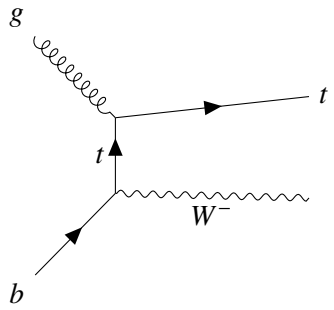

Figure 11: Representative leading-order Feynman diagrams of single top-quark production in association with a W boson.

section is calculated up to approximate next-to-next-to-next-to-leading order aN^{3}LO in QCD perturbation theory using soft-gluon corrections up to third order, matched to the full NLO calculation. At NLO, associated tW production interferes with leading order $t\bar{t}$ production and the subsequent decay $t \to Wb$. Different methods are used to remove or suppress contributions from $t\bar{t}$ and interference terms in order to partially isolate the tW process. The most common approaches are the diagram removal and diagram subtraction techniques [30]. The NLO calculation used here is done using MadGraph5_aMC@NLO [31] together with the diagram subtraction scheme. The central values for μ_r and μ_f are set to $m_{top} = 172.5$ GeV, while the uncertainty is estimated by varying both scales simultaneously by a factor of two up and down. The results for the MSHT2020 PDF set are presented in the original publication. The results for the PDF4LHC21 PDF sets are shown in the next section.

4.1 LHC Top WG recommendation

In Table 24, the definition of the scale and its uncertainty, the nominal PDF and its uncertainty, and the top-quark mass and its uncertainty are shown. The recommended cross-sections are given below in Table 25. The uncertainties include scale, PDF+α_s, m_{top} and E_{Beam} terms. The recommendation for most analyses is to add the scale and PDF+α_s uncertainties together and quote them as the total uncertainty. Analyses such as searches or precision measurements can also add the m_{top} and E_{Beam} terms in quadrature.

Table 24: Summary of the settings for the tW-channel recommendations.

Setting	Value	Uncertainty Definition
Scale	$\mu_r = \mu_f = 172.5$	7 point envelope
PDF	PDF4LHC21	Hessian approach
Top-Quark Mass (m_{top})	172.5 GeV	± 1.0 GeV

Table 25: The prediction values for $\sigma(tW)$ in pb using the PDF4LHC21 PDF set as input, together with the uncertainties from scale, PDF, α_s, mass and beam energy variations. The total uncertainty is given by adding scale and PDF uncertainties in quadrature.

Mode	Central value	Scale	PDF $\oplus$ α_s	Total	m_{top}	E_{Beam}
$\sigma(tW^+ + \bar{t}W^-)$	6.54	+0.16/-0.14	± 0.33	+0.37/-0.36	-0.13/+0.14	+0.02/-0.02

(a) 5.02 TeV

Mode	Central value	Scale	PDF $\oplus$ α_s	Total	m_{top}	E_{Beam}
$\sigma(tW^+ + \bar{t}W^-)$	17.1	+0.4 / -0.3	± 0.7	+0.8 / -0.8	-0.3 / +0.4	+0.1 / -0.1

(b) 7 TeV

Mode	Central value	Scale	PDF $\oplus$ α_s	Total	m_{top}	E_{Beam}
$\sigma(tW^+ + \bar{t}W^-)$	24.4	+0.6 / -0.5	± 0.9	+1.1 / -1.0	-0.4 / +0.4	+0.1 / -0.1

(c) 8 TeV

Mode	Central value	Scale	PDF $\oplus$ α_s	Total	m_{top}	E_{Beam}
$\sigma(tW^+ + \bar{t}W^-)$	79.3	+1.9 / -1.8	± 2.2	+2.9 / -2.8	-1.2 / +1.2	+0.2 / -0.2

(d) 13 TeV

Mode	Central value	Scale	PDF $\oplus$ α_s	Total	m_{top}	E_{Beam}
$\sigma(tW^+ + \bar{t}W^-)$	87.9	+2.0 / -1.9	± 2.4	+3.1 / -3.1	-1.3 / +1.3	+0.2 / -0.2

(e) 13.6 TeV

Mode	Central value	Scale	PDF $\oplus$ α_s	Total	m_{top}	E_{Beam}
$\sigma(tW^+ + \bar{t}W^-)$	93.8	+2.2 / -2.1	± 2.5	+3.3 / -3.3	-1.4 / +1.4	+0.2 / -0.2

(f) 14 TeV

Table 26: Mass parametrisation for the tW-production cross-sections for different center-of-mass energies.

Mode	a_0	a_1
$\sigma(tW^+ + \bar{t}W^-)$	0.661	-0.363

(a) 5.02 TeV

Mode	a_0	a_1
$\sigma(tW^+ + \bar{t}W^-)$	1.141	-15.709

(b) 7 TeV

Mode	a_0	a_1
$\sigma(tW^+ + \bar{t}W^-)$	1.037	0.312

(c) 8 TeV

Mode	a_0	a_1
$\sigma(tW^+ + \bar{t}W^-)$	1.659	-16.356

(d) 13 TeV

Mode	a_0	a_1
$\sigma(tW^+ + \bar{t}W^-)$	1.399	-2.413

(e) 13.6 TeV

Mode	a_0	a_1
$\sigma(tW^+ + \bar{t}W^-)$	1.395	-5.774

(f) 14 TeV

Table 27: Energy parametrisation for tW-production cross-sections. The coefficients a_i ($i \in \{0, ..., 6\}$) represent the free parameters from the energy parametrisation in Eq. (4).

Mode	a_0	a_1	a_2	a_3	a_4	a_5	a_6
$\sigma(tW^+ + \bar{t}W^-)$	-3.827	0.120	0.489	-1.386	0.045	0.176	-0.203

5 s-channel single top-quark production

This section presents results for single top-quark production in the s-channel. An example LO Feynman diagram is shown in Figure 12. Details of the calculation of the inclusive cross-sections are given in Ref. [6].

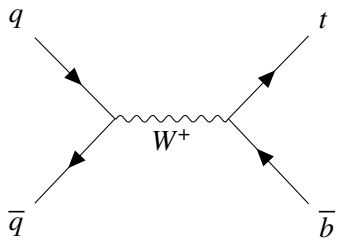

Figure 12: Representative leading-order Feynman diagrams of s-channel single top-quark production.

Here, the cross-section is calculated at NNLO in QCD perturbation theory. The central values for μ_r and μ_f are set to m_{top} =172.5 GeV and the W-boson mass is set to m_W = 80.385 GeV. Scale uncertainties are estimated by varying both scales simultaneously up and down by a factor of two. The PDF uncertainties are calculated using PDF4LHC21. The uncertainties are evaluated using replicas in contrast to the Hessian approach, which is used for the other channels. Given the small cross-section and the minor importance of this process as a background, uncertainties related to the top-quark mass and beam energy have not been calculated, but could be derived from the provided parameterisations.

5.1 LHC Top WG recommendation

In Table 28, the definitions of the scale and its uncertainty, the nominal PDF and its uncertainty, and the top-quark mass and its uncertainty are shown. The recommended cross-sections are given below in Table 29. The uncertainties include scale variations and PDF uncertainties using PDF4LHC21.

Table 28: Summary of the settings for the s-channel recommendations.

Setting	Value	Uncertainty Definition
Scale	$\mu_r = \mu_f = 172.5$	7 point envelope
PDF	PDF4LHC21	PDF replicas
Top-Quark Mass (m_{top})	172.5 GeV	None

Table 29: The predicted values for $\sigma(t\bar{b})$, $\sigma(\bar{t}b)$, and $\sigma(t\bar{b}+\bar{t}b)$ in pb using the PDF4LHC21 PDF as input, together with the uncertainties from scale variations and PDF uncertainties. The total uncertainty is given by adding scale and PDF uncertainties in quadrature.

Mode	Central value	Scale	PDF	Total
$\sigma(t\bar{b})$	1.823	+0.018 / -0.026	±0.048	+0.051 / -0.055
$\sigma(\bar{t}b)$	0.912	+0.011 / -0.012	±0.023	+0.025 / -0.026
$\sigma(t\bar{b}+\bar{t}b)$	2.736	+0.029 / -0.0373	±0.068	+0.074 / -0.078

(a) 5.02 TeV

Mode	Central value	Scale	PDF	Total
$\sigma(t\bar{b})$	2.993	+0.022 / -0.029	±0.067	+0.071 / -0.073
$\sigma(\bar{t}b)$	1.636	+0.011 / -0.018	±0.035	+0.037 / -0.039
$\sigma(t\bar{b}+\bar{t}b)$	4.629	+0.033 / -0.047	±0.098	+0.103 / 0.109

(b) 7 TeV

Mode	Central value	Scale	PDF	Total
$\sigma(t\bar{b})$	3.605	+0.032 / -0.025	±0.075	+0.082 / -0.079
$\sigma(\bar{t}b)$	2.029	+0.024 / -0.012	±0.042	+0.048 / -0.044
$\sigma(t\bar{b}+\bar{t}b)$	5.634	+0.055 / –0.037	±0.111	+0.124 / -0.177

(c) 8 TeV

Mode	Central value	Scale	PDF	Total
$\sigma(t\bar{b})$	6.828	+0.049 / -0.018	±0.112	+0.122 / -0.113
$\sigma(\bar{t}b)$	4.245	+0.035 / -0.012	±0.067	+0.076 / -0.068
$\sigma(t\bar{b}+\bar{t}b)$	11.073	+0.083 / -0.029	±0.174	+0.193 / -0.176

(d) 13 TeV

Mode	Central value	Scale	PDF	Total
$\sigma(t\bar{b})$	7.244	+0.041 / -0.026	±0.117	+0.124 / -0.120
$\sigma(\bar{t}b)$	4.534	+0.029 / -0.022	±0.070	+0.076 / -0.073
$\sigma(t\bar{b}+\bar{t}b)$	11.778	+0.070 / -0.049	±0.181	+0.194 / -0.188

(e) 13.6 TeV

Mode	Central value	Scale	PDF	Total
$\sigma(t\bar{b})$	7.495	+0.056 / -0.014	±0.119	+0.132 / -0.120
$\sigma(\bar{t}b)$	4.732	+0.036 / -0.014	±0.072	+0.080 / -0.073
$\sigma(t\bar{b}+\bar{t}b)$	12.227	+0.092 / -0.028	±0.186	+0.208 / -0.188

(f) 14.0 TeV

Table 30: Mass parametrization for the $t\bar{b}, \bar{t}b$, and $t\bar{b} + \bar{t}b$ production cross sections for different center-of-mass energies.

Mode	a_0	a_1
$\sigma(t\bar{b})$	0.159	-0.207
$\sigma(\bar{t}b)$	-0.059	1.252
$\sigma(t\bar{b} + \bar{t}b)$	0.079	0.078

(a) 5.02TeV

Mode	a_0	a_1
$\sigma(t\bar{b})$	0.130	-1.033
$\sigma(\bar{t}b)$	-0.155	1.202
$\sigma(t\bar{b} + \bar{t}b)$	0.028	0.234

(b) 7TeV

Mode	a_0	a_1
$\sigma(t\bar{b})$	-0.064	0.338
$\sigma(\bar{t}b)$	-0.366	0.799
$\sigma(t\bar{b} + \bar{t}b)$	-0.165	0.631

(c) 8TeV

Mode	a_0	a_1
$\sigma(t\bar{b})$	0.361	1.206
$\sigma(\bar{t}b)$	0.205	-1.818
$\sigma(t\bar{b} + \bar{t}b)$	0.307	-0.249

(d) 13TeV

Mode	a_0	a_1
$\sigma(t\bar{b})$	0.338	-0.561
$\sigma(\bar{t}b)$	0.171	-0.579
$\sigma(t\bar{b} + \bar{t}b)$	0.283	-1.050

(e) 13.6TeV

Mode	a_0	a_1
$\sigma(t\bar{b})$	0.367	0.320
$\sigma(\bar{t}b)$	0.189	0.582
$\sigma(t\bar{b} + \bar{t}b)$	0.300	0.274

(f) 14TeV

Table 31: Energy parametrisation for $t\bar{b}, \bar{t}b$, and $t\bar{b} + \bar{t}b$ cross-sections. The coefficients a_i ($i \in \{0, ..., 6\}$) represent the free parameters from the energy-parametrisation in Eq. (4).

Mode	a_0	a_1	a_2	a_3	a_4	a_5	a_6
$\sigma(t\bar{b})$	0.031	0.441	0.007	-0.017	-0.048	-0.000	-0.016
$\sigma(\bar{t}b)$	0.130	-0.052	0.027	0.121	0.008	-0.024	0.012
$\sigma(t\bar{b} + \bar{t}b)$	0.831	0.078	0.053	0.016	-0.151	-0.028	0.013

6 Conclusion

This note presents cross-section predictions at the highest available precision for all three SM single top-quark processes. The t-channel cross-sections are calculated for different PDF sets using MCFM. They are quoted for all centre-of-mass energies relevant for the LHC, namely 5.02 TeV , 7 TeV , 8 TeV , 13 TeV , 13.6 TeV , and 14 TeV . The cross-sections for the other two single top-quark processes are provided directly by the authors of the calculations for all of the above centre-of-mass energies. LHCtopWG recommendations of the predicted cross-sections based on the PDF4LHC21 PDF sets are given together with recommended uncertainties on α_s, PDF, and scale variations. Searches or precision measurements should also account for mass and energy dependencies where needed. In addition mass and energy parametrisations are also provided for all the processes. Figure 13 summarizes the cross-sections presented in this note for the t-channel, tW-channel, and s-channel processes across all centre-of-mass energies considered by showing the derived parametrisations for the $\sqrt{s}$ dependence of the individual processes.

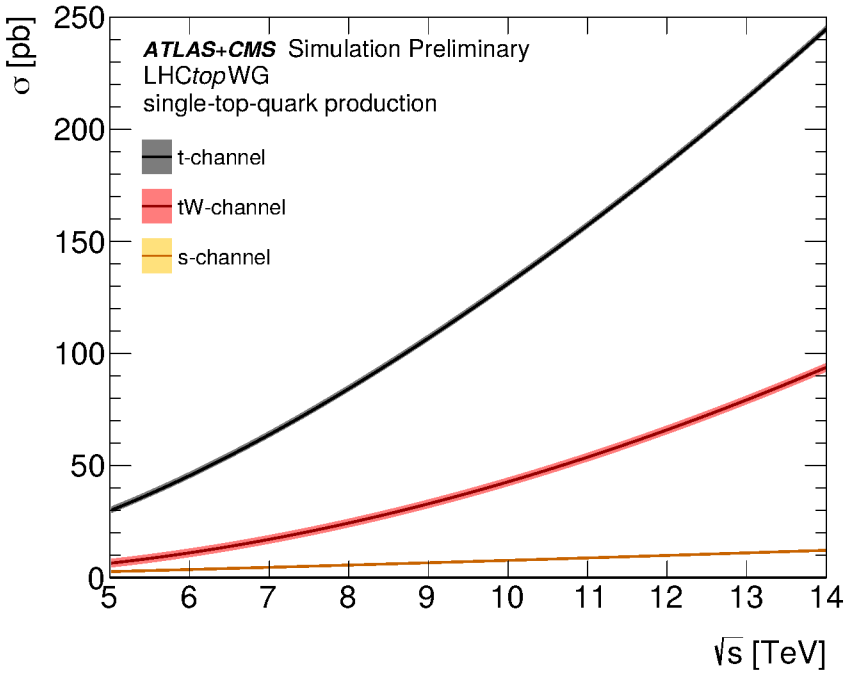

Figure 13: Parametrisation for the energy dependence of the t-channel, tW-channel and s-channel cross-section in pb. For all processes, except the s-channel, the scale, α_s and PDF uncertainties are included. The s-channel only includes scale and PDF uncertainties.

References

[1] P. Kant et al., *HatHor for single top-quark production: Updated predictions and uncertainty estimates for single top-quark production in hadronic collisions*, Comput. Phys. Commun. **191** (2015) 74, arXiv: 1406.4403 [hep-ph] (cit. on p. 2).

[2] M. Brucherseifer, F. Caola and K. Melnikov, *On the NNLO QCD corrections to single-top production at the LHC*, Phys. Lett. B **736** (2014) 58, arXiv: 1404.7116 [hep-ph] (cit. on p. 2).

[3] E. L. Berger, J. Gao, C. Yuan and H. X. Zhu, *NNLO QCD Corrections to t-channel Single Top-Quark Production and Decay*, Phys. Rev. **D94** (2016) 071501, arXiv: 1606.08463 [hep-ph] (cit. on p. 2).

[4] J. Campbell, T. Neumann and Z. Sullivan, *Single-top-quark production in the t-channel at NNLO*, JHEP **02** (2021) 040, arXiv: 2012.01574 [hep-ph] (cit. on pp. 2, 8).

[5] N. Kidonakis and N. Yamanaka, *Higher-order corrections for tW production at high-energy hadron colliders*, JHEP **05** (2021) 278, arXiv: 2102.11300 [hep-ph] (cit. on pp. 2, 28).

[6] Z. L. Liu and J. Gao, *s -channel single top quark production and decay at next-to-next-to-leading-order in QCD*, Phys. Rev. D **98** (2018) 071501, arXiv: 1807.03835 [hep-ph] (cit. on pp. 2, 30).

[7] J. Campbell and T. Neumann, *Precision Phenomenology with MCFM*, JHEP **12** (2019) 034, arXiv: 1909.09117 [hep-ph] (cit. on pp. 2, 8).

[8] S. Alekhin, J. Blümlein, S. Moch and R. Placakyte, *Parton distribution functions, α_s, and heavy-quark masses for LHC Run II*, Phys. Rev. D **96** (2017) 014011, arXiv: 1701.05838 [hep-ph] (cit. on p. 3).

[9] T.-J. Hou et al., *Progress in the CTEQ-TEA NNLO global QCD analysis*, (2019), arXiv: 1908.11394 [hep-ph] (cit. on p. 3).

[10] S. Bailey, T. Cridge, L. A. Harland-Lang, A. D. Martin and R. S. Thorne, *Parton distributions from LHC, HERA, Tevatron and fixed target data: MSHT20 PDFs*, Eur. Phys. J. C **81** (2021) 341, arXiv: 2012.04684 [hep-ph] (cit. on p. 3).

[11] R. D. Ball et al., *Parton distributions for the LHC run II*, JHEP **04** (2015) 040, arXiv: 1410.8849 [hep-ph] (cit. on p. 3).

[12] R. D. Ball et al., *Parton distributions from high-precision collider data*, Eur. Phys. J. C **77** (2017) 663, arXiv: 1706.00428 [hep-ph] (cit. on pp. 3, 5).

[13] NNPDF Collaboration, R. D. Ball et al., *The path to proton structure at 1% accuracy*, Eur. Phys. J. C **82** (2022) 428, arXiv: 2109.02653 [hep-ph] (cit. on p. 3).

[14] H. Abramowicz et al., *Combination of measurements of inclusive deep inelastic $e^{\pm}p$ scattering cross sections and QCD analysis of HERA data*, Eur. Phys. J. C **75** (2015) 580, arXiv: 1506.06042 [hep-ex] (cit. on p. 3).

[15] ATLAS Collaboration, *Precision measurement and interpretation of inclusive W^+, W^- and Z/γ^* production cross sections with the ATLAS detector*, Eur. Phys. J. C **77** (2017) 367, arXiv: 1612.03016 [hep-ex] (cit. on p. 3).

[16] ATLAS Collaboration, *Determination of the parton distribution functions of the proton from ATLAS measurements of differential W and Z/γ^* boson and $t\bar{t}$ cross sections*, ATL-PHYS-PUB-2018-017, 2018, URL: https://cds.cern.ch/record/2633819 (cit. on p. 3).

[17] ATLAS Collaboration, *Determination of the parton distribution functions of the proton using diverse ATLAS data from pp collisions at $\sqrt{s} = 7, 8$ and 13 TeV*, Eur. Phys. J. C **82** (2021) 438, arXiv: 2112.11266 [hep-ex] (cit. on p. 3).

[18] P. Nason, *A new method for combining NLO QCD with shower Monte Carlo algorithms*, JHEP **11** (2004) 040, arXiv: hep-ph/0409146 (cit. on p. 4).

[19] R. Frederix, E. Re and P. Torrielli, *Single-top t-channel hadroproduction in the four-flavour scheme with POWHEG and aMC@NLO*, JHEP **09** (2012) 130, arXiv: 1207.5391 [hep-ph] (cit. on p. 4).

[20] J. M. Campbell, J. Huston and W. Stirling, *Hard Interactions of Quarks and Gluons: A Primer for LHC Physics*, Rept. Prog. Phys. **70** (2007) 89, arXiv: hep-ph/0611148 (cit. on p. 5).

[21] S. Carrazza, S. Forte, Z. Kassabov, J. I. Latorre and J. Rojo, *An Unbiased Hessian Representation for Monte Carlo PDFs*, Eur. Phys. J. C **75** (2015) 369, arXiv: 1505.06736 [hep-ph] (cit. on p. 5).

[22] S. Dulat et al., *New parton distribution functions from a global analysis of quantum chromodynamics*, Phys. Rev. D **93** (2016) 033006, arXiv: 1506.07443 [hep-ph] (cit. on p. 5).

[23] E. Todesco and J. Wenninger, *Large Hadron Collider momentum calibration and accuracy*, Phys. Rev. Accel. Beams **20** (2017) 081003 (cit. on p. 6).

[24] M. Czakon, P. Fiedler and A. Mitov, *Total Top-Quark Pair-Production Cross Section at Hadron Colliders Through $O(\alpha_S^4)$*, Phys. Rev. Lett. **110** (2013) 252004, arXiv: 1303.6254 [hep-ph] (cit. on p. 6).

[25] U. Langenfeld, S. Moch and P. Uwer, *New results for t anti-t production at hadron colliders*, (2009) 131, arXiv: 0907.2527 [hep-ph] (cit. on p. 7).

[26] J. Campbell, T. Neumann and Z. Sullivan, *Testing parton distribution functions with t-channel single-top-quark production*, Phys. Rev. D **104** (2021) 094042, arXiv: 2109.10448 [hep-ph] (cit. on p. 8).

[27] T. Stelzer, Z. Sullivan and S. Willenbrock, *Single top quark production via W - gluon fusion at next-to-leading order*, Phys. Rev. D **56** (1997) 5919, arXiv: hep-ph/9705398 (cit. on p. 8).

[28] F. Maltoni, G. Ridolfi and M. Ubiali, *b-initiated processes at the LHC: a reappraisal*, JHEP **07** (2012) 022, [Erratum: JHEP 04, 095 (2013)], arXiv: 1203.6393 [hep-ph] (cit. on p. 8).

[29] A. Buckley, J. Ferrando, S. Lloyd, K. Nordström, B. Page et al., *LHAPDF6: parton density access in the LHC precision era*, Eur. Phys. J. C **75** (2015) 132, arXiv: 1412.7420 [hep-ph] (cit. on p. 8).

[30] T. M. P. Tait, *The tW^- mode of single top production*, Phys. Rev. D **61** (1999) 034001, arXiv: hep-ph/9909352 (cit. on p. 28).

[31] J. Alwall et al., *The automated computation of tree-level and next-to-leading order differential cross sections, and their matching to parton shower simulations*, JHEP **07** (2014) 079, arXiv: 1405.0301 [hep-ph] (cit. on p. 28).